ACADEMIC PRESS

Available online at www.sciencedirect.com

SCIENCE DIRECT®

Journal of Sound and Vibration 262 (2003) 1009–1046

JOURNAL OF SOUND AND VIBRATION

www.elsevier.com/locate/jsvi

Influence of adaptive control on vortex-driven instabilities in a scaled model of solid propellant motors

J. Anthoine[a,*], M. Mettenleiter[b], O. Repellin[a], J.-M. Buchlin[a], S. Candel[b]

[a] *von Karman Institute for Fluid Dynamics, Chaussee de Waterloo 72, 1640 Rhode-St-Genese, Belgium*
[b] *Laboratoire E.M2.C, CNRS, Ecole Centrale Paris, 92295 Chatenay-Malabry Cedex, France*

Received 9 February 2001; accepted 14 February 2002

Abstract

Aeroacoustic instabilities occur in many applications of technological interest and have undesirable effects on the steady operation of the system. Passive and active means are sought to reduce the level of oscillation and eliminate the instability. In the case of segmented solid rocket motors, observations indicate that low-frequency oscillations are generated by a coupling between vortex shedding in shear regions established in the flow and the acoustic eigenmodes of the system. This process is investigated in this article on a model-scale configuration representing the geometry of the motor. An active control loop is exploited to obtain resonant and non-resonant conditions for the same operating point. Adaptive techniques are used to stabilize the flow and the experiment serves as a testbed for active control. It is shown that an adaptive system may be applied to essentially suppress the pressure oscillations. The instability mechanism is then studied by analyzing the flow field with particle image velocimetry. It is found that control noticeably modifies the mean flow structure. Detailed studies of the vortex pattern in the shedding region indicate that the concentrated vorticity and the corresponding circulation values remain in the same range but that vorticity is shed more randomly when the resonance is eliminated by the controller. This indicates that control is achieved by reducing the level of organization in the vortex pattern. Under resonant conditions the level of pressure fluctuations results from coherent interactions between vortices and the downstream nozzle. This process feeds energy in one of the acoustic modes of the system enhancing the pressure level. It is made less effective by the control loop.

1. Introduction

Aeroacoustic instabilities occur in a wide range of technical applications. The resulting oscillations are sometimes wanted in systems designed to produce the periodic motion efficiently

*Corresponding author. Tel.: +32-2-359-96-15; fax: +32-2-359-96-00.
E-mail address: anthoine@vki.ac.be (J. Anthoine).

0022-460X/03/$ - see front matter
PII: S0022-460X(02)01034-9

as in musical instruments. In most cases, aeroacoustic instabilities perturb the operation and have to be suppressed. This article describes experiments aiming at the active reduction of aeroacoustic instabilities by adaptive techniques. We will specifically analyze the effect of control on the structure of the flow using detailed measurements and in particular particle image velocimetry. The present study focuses on a specific class of instabilities involving vortex shedding and acoustic resonances. These instabilities have received considerable attention in the past 20 years in relation with developments of large solid propellant motors for space vehicles and launchers. The phenomenon develops in the confined flow established in the motor and involves a coupling between vortex shedding and longitudinal acoustic resonant motion. The motor usually features a set of solid propellant grains separated by inhibitor rings ensuring thermal protection (see Fig. 1). There are three propellant segments in the Ariane 5 solid propellant accelerators (P-230). Propellant is consumed during the flight at a rate which exceeds that of the separation rings (also designated as inhibitor rings). Regression of the burning surface is faster than the consumption of the inhibitor. The inhibitor rings protrude in the flow after a certain time producing regions of high shear where vortex shedding may be generated. This mechanism drives oscillation if the shedding is coupled to one of the acoustic resonant modes of the motor chamber.

A considerable amount of experimental data has been gathered on full-scale rockets (Space Shuttle and Titan 4) static tests or in flight (see Refs. [1–4]). Pressure oscillations at frequencies close to those of the first two longitudinal eigenmodes were also found during the development full-scale static hot fire tests of the Ariane-5 solid propellant motors. Vortex-driven acoustically coupled oscillations were later observed on sub-scale model rockets (see Refs. [5–7]). These various studies point out that the frequency of oscillation decreases as the grain surface regresses. This observation typifies processes which depend on the velocity of the flow. Observations also indicate that the pressure oscillations reach a maximum when the vortex shedding frequency is close to one of the natural frequencies of the motor chamber.

An early interpretation of the phenomenon is due to Flandro [8], who linked the oscillations to the hydrodynamic instability of the sheared regions of the flow and to the coupled response of the motor. This viewpoint is supported by experiments at various scales and for a variety of geometries and operating conditions. It is now well established that unstable oscillations are

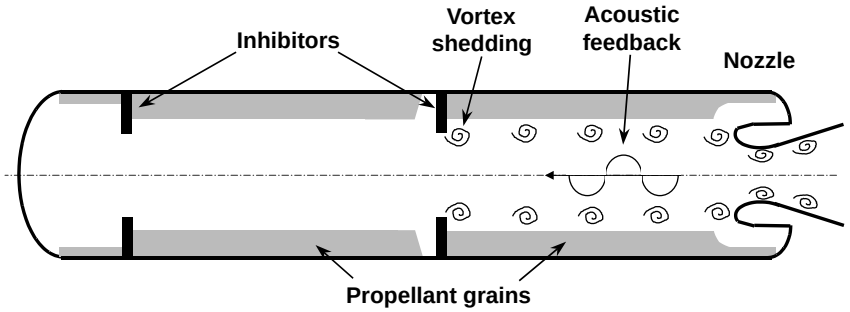

Fig. 1. Internal geometry of the Ariane 5 solid rocket motor and flow-acoustic coupling.

produced by the combination of the following mechanisms (see Fig. 1) [9,10,4]: a hydrodynamic instability of shear regions of the flow; the roll-up, growth and advection of vortices; impingement of the vortices on a surface located downstream such as the nozzle head and generation of an acoustic perturbation; acoustic propagation from the downstream source; transfer of energy from the acoustic mode to the shear flow instability.

The hydrodynamic instability created by the inhibitor leads to vortex formation. The coherence degree of these structures depends on the presence of an external acoustic field. When the vortices hit a surface like the nozzle head a dipole source is generated and energy passes from the vortex to the acoustic field. This energy is fed back to the shear flow instability by one of the acoustic modes of the system. The receptivity of the shear region to external modulations closes the loop and a new vortex is shed and advected downstream. Three frequencies must be considered in the process: the characteristic frequencies of the shear layer, f_s; the feedback frequencies of the impinging shear layer, f_b; the acoustic resonance frequencies of the full system, f_a.

Among the available shear layer frequencies, f_s is selected by a feedback mechanism involving an interaction of the shear layer with the downstream end of the system. The characteristic length scale is the distance l between the shear layer origin and the impingement point. The feedback frequency f_b is obtained if certain phase relations are satisfied. It is generally agreed that this frequency is determined by the expression [11–13,4]

$$mT = \frac{l}{U_c} + \frac{l}{c - U} + \tau, \tag{1}$$

where $T = 1/f_b$ is the period of the process, m is the number of vortices at a given instant between the shedding region and the impingement surface separated by a distance l. U and U_c are the flow velocity and the vortex transport velocity, respectively. c is the speed of sound and τ designates the delay between the vortex impingement and the generation of a pressure pulse at the downstream surface. One generally assumes that τ may be expressed as a fraction of the period, $\tau = \alpha T$, and that the transport velocity is proportional to the flow velocity, $U_c = kU$. Upon using these expressions and assuming that the Mach number of the flow is small, the feedback frequency is given by

$$f_b \simeq \frac{U}{l}\left(\frac{m - \alpha}{M + 1/k}\right). \tag{2}$$

This expression was first obtained by Rossiter [11] in an analysis of acoustic radiation by an airflow over a cavity. Its application to segmented solid rockets provides a suitable estimate of the frequencies observed (see for example Ref. [4] for a clear validation). Data also indicate that the pressure oscillation reaches large amplitudes when the feedback frequency f_b, given by Eq. (2), matches one of the eigenfrequencies f_a of an acoustic mode of the system ($f_b \simeq f_a$). Other experiments indicate that the process is also controlled by the relative positions of the vortex shedding region and the acoustic resonant mode structure [3,14]. In general the acoustic mode triggers vortex shedding more effectively at locations where the pressure features a node and the velocity an anti-node.

Numerical simulations [15–18] carried out in the last 10 years have brought further information on the aeroacoustic processes which lead to vortex-driven oscillations in solid rocket motors. Simulations show that vortices may also develop from edges of the solid propellant (for example, from the upstream edge of a cavity separating two segments or from the downstream edge of the last segment). The bending flow resulting from the propellant combustion also features a natural instability which is potentially capable of generating vortices [19]. These findings are supported by hot and cold flow experiments [20].

Because combustion is believed to take a minor part in the instability mechanism, most laboratory experiments were carried out with models operating with cold gases. A configuration involving a duct with one or two diaphragms is used for example by Culick [21], Dunlap [14], Hourigan [22], Huang [23], Planquart [24], Anthoine [25], Mettenleiter [26], Stubos [27] and Anthoine et al. [28]. The vortex shedding is produced at the upstream diaphragm and the duct acts as a resonator through its natural eigenmodes. Culick [21] showed that the resonant oscillation could not be sustained with a single diaphragm. An obstacle located downstream of the shedding point is required and serves to transfer energy from the impinging vortices into the resonant acoustic mode [29,30]. Another set-up designed by Couton [31] features a rectangular two-dimensional channel with wall injection, obstacles simulating inhibitor baffles and a submerged nozzle. The channel resonance was linked to the excitation of the first longitudinal modes and the amplification of the acoustic level was found to depend on the injected mass flow rate.

In the present study an axisymmetric duct representing the geometry of the real motor is used. Such an axial cold flow model includes only one inhibitor where the vortices are formed, and a submerged nozzle where the vortices collide and generate sound. This configuration correctly simulates the interaction of the advected vortices with the nozzle head. An active control device implemented with a sensor, an actuator and an adaptive controller is fitted to the system to suppress the pressure oscillations when needed. It is thus possible to study a naturally resonant flow under non-resonant conditions. The operating parameters remaining fixed, the control system is switched on and the acoustic pressure oscillation is suppressed. One may then examine the changes in the flow pattern induced by the presence or absence of acoustic resonance. This is done with particle image velocimetry downstream of the inhibitor. The combined use of a resonant model, active control and PIV is aimed at applying adaptive techniques to control aeroacoustic instability phenomena, providing new information on the processes leading to instability in a geometry which typifies the back end of a solid rocket motor, and getting an understanding of how the controller modifies the flow to reduce the pressure oscillations.

Because active control of the flow is an essential aspect of this study it is worth giving a brief overview of research in this area. Since the subject is quite broad, we will consider only the topic of instability control. Control of combustion instability using feedback concepts is suggested in the early work of Tsien [32], Crocco [33] and Marble [34]. Practical demonstrations have been completed more recently by Dines [35], Heckl [36], Bloxsidge et al. [37] and Lang et al. [38]. A review of this subject is given by McManus et al. [39]. Active control of flow instabilities was demonstrated experimentally by Roussopoulos [40]. Closed loop control experimental demonstrations have concerned flow over cavities, aeroacoustic resonances in ducts [23,26], vortex shedding in low Reynolds number flows [40], impacting flows [41], compressor surge [42], etc.

Most of the earlier work was based on fixed parameter controllers and had a limited range of applicability. Because combustion or flow instabilities change with the operating parameters, it is important to use adaptive techniques to achieve control over a broad range of flow conditions. This point was demonstrated by Billoud et al. [43] and later by Koshigoe et al. [44]. Adaptive techniques have led to many applications in the control of sound and vibration, a subject of considerable technical importance which has been investigated extensively [45,46]. It is believed that technical applications in flow control will require self-adjusting systems of the kind tested in this article.

The paper begins with a brief presentation of the methods used to identify and characterize vortices in a flow field (Section 2). These methods will be used later in this article to examine the flow structure. The experimental configuration is then described (Section 3). Some aspects are only briefly covered because they are discussed in more detail in other publications [25,26]. The results of three experiments are reported in Section 4. A low speed case which is naturally free of oscillation is considered. After that, a higher speed case which is naturally resonant is envisioned. When control is applied to this flow, resonance vanishes. The flow patterns in the three cases are examined with particle image velocimetry (PIV). The data are used in Section 4 to describe the changes which take place under controlled operation and to improve the current view of the process leading to instability.

2. Characterization and identification of vortices

The study of coherent structures in turbulent flows remains a central subject in fluid dynamics. A "universal definition" of coherent structures is still missing. Coherent patterns of a particular flow have common features but they are far from being identical. Moreover, they do not appear with precise regularity in time and space. This lack of regularity makes them so difficult to be defined and described. According to Robinson [47] "a vortex exists when instantaneous streamlines mapped onto a plane normal to the vortex core exhibit a roughly circular or spiral pattern, when viewed from a reference frame moving with the vortex core". Following Hussain [48] "a coherent structure is a connected turbulent fluid mass with instantaneously phase-correlated vorticity over its spatial extent". In other words, a vortex is a region where the instantaneous flow is rotating around its center, and which can be advected with a certain velocity. Coherent structures are three-dimensional and the random nature of turbulence makes their "signal-to-noise" ratio low. As a consequence, their eduction from noisy data is a difficult task.

2.1. Characteristics of a vortex

The vortices considered in this research are created by an annular obstacle. The vortex rings shed by the obstacle may not be perfectly axisymmetric but their behavior can still be investigated in a plane Oxy perpendicular to the vortex core (or nearly so). In this plane, the characteristic parameters of a vortex are mainly: the position of its center (x_0, y_0), its velocity distribution ($\boldsymbol{V} = \boldsymbol{u} + \boldsymbol{v}$), the transport velocity (u_v, v_v), diameter (D_v), vorticity peak (Ω), vorticity distribution

(ω), circulation (Γ) and enstrophy (E) where

$$\omega = \frac{\partial v}{\partial x} - \frac{\partial u}{\partial y}, \tag{3}$$

$$\Gamma = \oint \boldsymbol{v} \cdot \mathrm{d}l = \int\int \omega \, \mathrm{d}S, \tag{4}$$

$$E = \int\int \omega^2 \, \mathrm{d}S. \tag{5}$$

Among standard vortex models, the Oseen vortex is often used to typify vortex motion. The corresponding velocity distribution is, in polar co-ordinates r, θ:

$$v_\theta = \frac{\Gamma_0}{2\pi r}(1 - \mathrm{e}^{-r^2/\sigma^2}), \quad v_r = 0, \tag{6}$$

where σ is a characteristic dimension of the vortex. Fig. 2(a) shows the 2-D-pattern of such a vortex flow.

2.2. Identification of a vortex

Expression (6) should not be taken as an exact representation. It merely serves as a guide in the vortex identification process and it will be used to synthesize the data gathered. Jeong and Hussain [49] list the different criteria used until now to recognize vortex motion. First of all, the center of a vortex corresponds to a local pressure minimum. Unfortunately, a pressure map is difficult to obtain experimentally. A straightforward criterion is to detect the presence of a vorticity peak at the center of the pattern. Indeed, vorticity is a Galilean invariant of the velocity, which means that it is not affected by an additional transport velocity. However, while a center of a vortex leads to a peak of vorticity, a vorticity peak does not necessarily correspond to a vortex

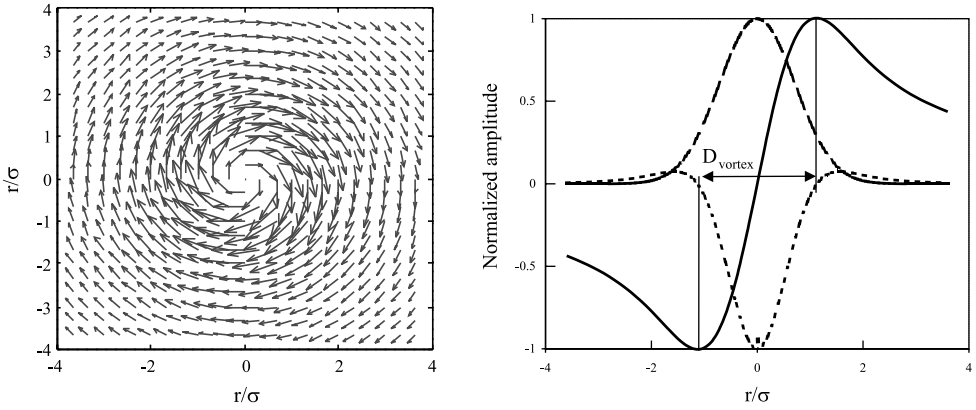

(a) 2D−pattern

(b) Velocity (———), vorticity (- - - -) and λ (·····) distributions along a diameter

Fig. 2. The Oseen vortex ($r^2 = x^2 + y^2$).

center, like, for example, in a shear layer. Thus, an analysis based on the vorticity field can be limited when studying a flow with obstacle. In the more elegant method presented by Jeong and Hussain [49] a vortex in an incompressible flow is defined in terms of the eigenvalues of the symmetric tensor $S^2+\Omega^2$, where S and Ω are, respectively, the symmetric and antisymmetric parts of the velocity gradient tensor ∇V (S and Ω are deformation and rotation tensors, respectively). In planar flows, the vortex core corresponds to a connected region within which $\lambda<0$, where λ is the non-zero eigenvalue of $S^2+\Omega^2$:

$$\lambda(x,y)=\left(\frac{\partial u}{\partial x}\right)^2+\left(\frac{\partial u}{\partial y}\right)\left(\frac{\partial v}{\partial x}\right)<0. \tag{7}$$

This criterion means that within a vortex the derivatives of the velocity components must be of opposite signs. Note that the formulation in cylindrical co-ordinates, more complex to be implemented, has been tested on typical images and led to very close results compared to the 2-D approximation given by Eq. (7). The diameter D_v of the vortex is defined by the zero crossing contour of λ. This contour corresponds to the maximum velocity in Oseen's vortex. Finally, the eigenvalue λ is Galilean invariant as well as the vorticity because it only involves velocity derivatives. Fig. 2(b) shows the velocity, vorticity and λ distributions along a diameter for an Oseen vortex. While the λ field is used for the identification of the vortex and for the determination of its diameter, the other characteristics, such as Γ and E are computed from the vorticity field.

2.3. Eduction of a vortex

Particle image velocimetry provides instantaneous velocity vector fields, as explained in Section 3.2. From these fields, the instantaneous vorticity and λ mappings can be computed and vortices can be detected from the λ contours. To make statistical averages on the vortices, their eduction from the flow field should be automatic and it is done here by using a wavelet analysis applied to the λ field. The vortex detection algorithm, based on the property of selectivity in space and scale of the continuous wavelet transform, allows one to determine the vortex position and size. The other characteristics can be calculated from these two informations. The processing of the wavelet transformation [50] is carried out to localize a specific scale (size of the vortex) within the 2-D λ-field signal (position of the vortex). The signature of a vortex in a λ map is a Gaussian curve detected by a 2-D wavelet designated as the "Mexican Hat". The mother wavelet is given by

$$\psi(x,y)=-(2-x^2-y^2)\mathrm{e}^{-(x^2+y^2)/2}. \tag{8}$$

More details about the wavelet analysis can be found in Ref. [51]. Fig. 3 shows the comparison between the λ field and the Mexican Hat. The point where the Mexican Hat crosses the zero axes defines the diameter of the vortex. The Mexican Hat and the λ distribution do not have exactly the same shapes. The relation between the diameter of the Mexican Hat and that of Oseen's vortex is obtained by calibration. From a PIV velocity vector field, the λ field is computed by a standard four points centered scheme. The Mexican Hat is dilated for different scales. Each scale scans the whole λ field. The convolution gives a 4-D information: 2-D for the location (x,y), 1-D for the scale (D_v), and 1-D for the wavelets coefficient ($|W|$) [52]. This last information allows detection of

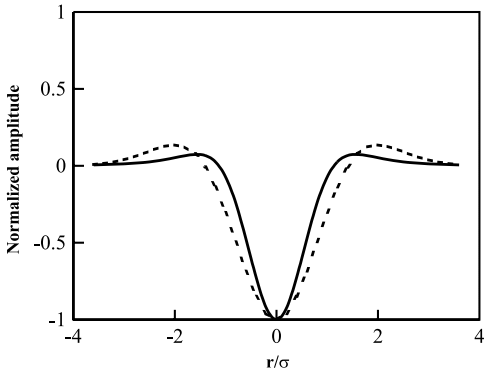

Fig. 3. Comparison between the λ field (—-) and the Mexican Hat (.....) ($r^2 = x^2 + y^2$).

a vortex if its value is higher than a chosen threshold, linked to the energy carried by the candidate coherent structure. In other words, the vortex detection algorithm yields the wavelet coefficient $|W|$ as a function of x, y and D_v; a large value of the coefficient implies a good fit between the wavelet of that scale and the data at that point. When a region of high values of the wavelet coefficient is identified by the vortex detection algorithm, the center of the vortex core corresponds to the local maximum of that coefficient. A vortex is identified if the following conditions are fulfilled: its enstrophy must be higher than a given percentage of the total enstrophy of the vorticity field and the vortex must not overlap a previously found vortex, i.e., the investigation is restricted to distinct vortices. Therefore, the wavelet coefficient values higher than the threshold but located within the scale D_v of the previously found vortex are not considered.

3. Experimental configuration

3.1. Experimental set-up

The experimental facility is composed of a cylindrical test section, a fan, and an orifice plate. The test section is designed to reproduce the geometry of the solid propellant accelerator of Ariane 5 (see Fig. 4). As indicated previously, the Ariane 5 accelerator is made of three propellant grains (Fig. 1). The first segment (S1) is active during the first 30 s of the combustion, while segments S2 and S3 are active during the total combustion time of 129 s. Therefore, by restricting the investigation to times larger than $T_c/4$, where T_c is the total combustion time, the head (S1) can be assumed inactive and replaced by an aerodynamically shaped inlet and a honeycomb to get a uniform one-dimensional flow. Behind the inlet, the set-up consists of two cylindrical segments, with an inhibitor, and a submerged nozzle. The internal diameter of the segments, equal to 0.15 m, is 1/15th model scale of the real motor when 50% of the propellant is burnt, and the dynamic similarity is achieved by matching the model and full-scale Mach numbers. Each of the two segments has a length $L/2$ of 0.63 m. The nozzle has a throat diameter of 0.059 m. Its geometry is sketched in Fig. 4. The main characteristic of this nozzle is the appearance of a cavity around the

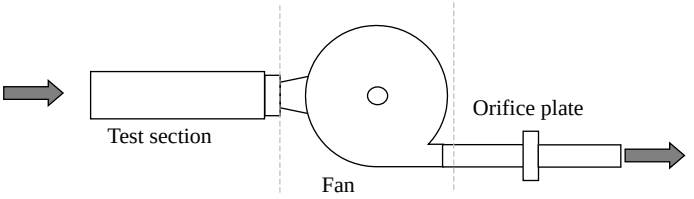

(a) Sketch of the experimental facility

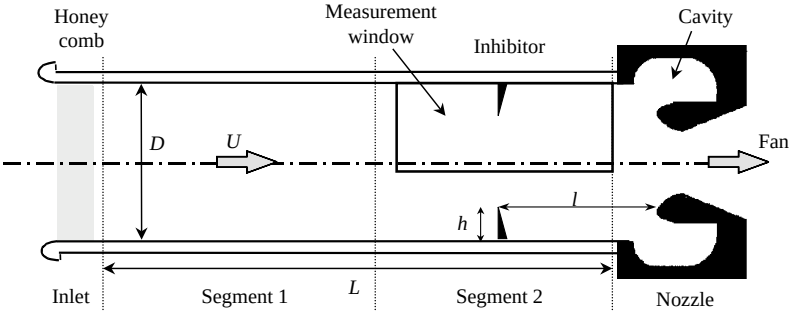

(b) Sketch of the test section

Fig. 4. Sketch of the experimental facility.

convergent section. During combustion, the cavity volume varies as explained in Ref. [53]. At 50% of the combustion process, the geometry is close to that drawn in Fig. 4. The total length of the test section including the inlet and the nozzle cavity is equal to 1.75 m. As the vortices are expected to generate sound when interacting with the nozzle, the inhibitor–nozzle distance l has to be small, in the case of an axial flow. This will guarantee that the vortices reach the nozzle. The value chosen for the inhibitor–nozzle distance of 0.14 m corresponds to an optimized flow-acoustic coupling [54]. The inhibitor has a thickness of 0.5 mm at the leading edge (2.5 mm at its base) and an internal diameter of 113.2 mm yielding an inhibitor height h of 17.4 mm. It is fixed by means of a thin silicon seal.

The flow is injected axially in the test section from the head-end (inlet). The model operates with a flow of cold air sucked by a fan placed downstream of the test section. The centrifugal fan produces a mean flow velocity U_0 in the test section varying from 8 to 28 m/s. This velocity is deduced from the mass flow rate measured with the orifice plate. The corresponding Reynolds number based on the inhibitor height h is changing from 9000 to 32 000.

3.2. Instrumentation and post-processing

A piezoelectric transducer model 106B50 from PCB Piezotronics Inc. is mounted in the test section for pressure fluctuation measurements. This unit is placed at the wall just upstream of the nozzle. A calibrated hot wire of 9 μm in diameter, built in-house, is also mounted between the inhibitor and the nozzle. The pressure sensor and the hot wire are connected to a spectrum

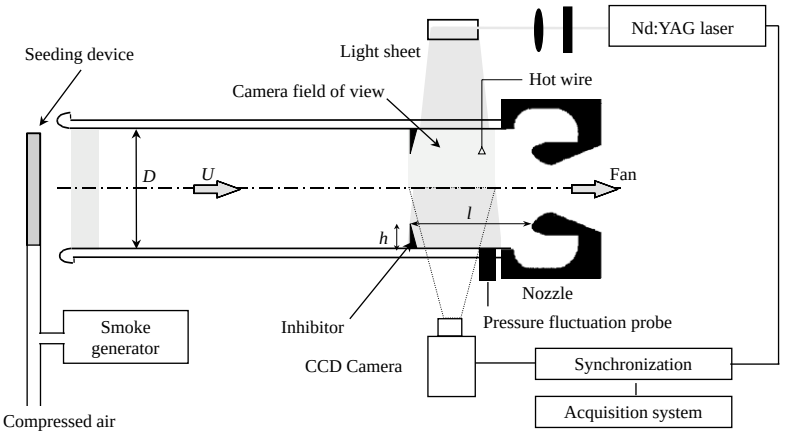

Fig. 5. Instrumentation for PIV measurements.

analyzer (Hewlett Packard model 35660) or to a DAS1601 acquisition card controlled by TESTPOINT^{TM}.

A Particle Image Velocimetry (PIV) technique is used to measure the velocity field between the inhibitor and the nozzle. For such experiments, the test section consists of a Plexiglas^{TM} tube of 25 mm thickness. Repellin [55] has shown that such a thickness is not suitable for PIV measurements because of optical distortion. To avoid this difficulty, the Plexiglas^{TM} tube is replaced by a Makrolon^{TM} tube of 1 mm thickness on a length of 0.59 m from the nozzle. The laser sheet and the camera are placed in front of the thin tube. Tests prove that such a thickness is sufficiently small to reduce optical distortion to an acceptable level. Fig. 5 shows a schematic of the PIV instrumentation. The light sheet is generated by a Nd:YAG double pulsed laser, operating at 10 Hz and a set of cylindrical lenses. The laser provides 4 ns pulses with energy of 400 mJ. A TSI cross-correlation CCD camera model 630044 (640 × 480 pixels) records the successive images which are acquired and saved by the TSI acquisition software INSIGHT^{TM}. The optical calibration in both directions is achieved by measuring the field of view of the CCD camera at the location of the laser sheet. The PIV field of view of 98 × 76 mm is situated just downstream of the inhibitor. The laser working at 10 Hz and the camera operating at 30 Hz are synchronized by the TSI unit 610030. The synchronizer is also used to set a time delay ΔT between the two laser pulses of around 50 μs, depending on the flow velocity.

Because of the stagnation region at the end of the recirculation bubble, the use of standard oil in the form of seeding droplets leads to a film deposit on the wall behind the inhibitor and through which the camera is looking. To reduce this effect, oil has been replaced by the global mix smoke fluid manufactured by Le Maitre Ltd. (England), which has the property to condense less. Moreover, an additional supply of compressed air is also injected after the smoke generator and the mixture is introduced in the flow by means of a vertical tube comprising several small orifices, placed in front of the test section. This improves mixing with air and the uniformity of the seeding.

Two successive images are processed with the cross-correlation program WiDIM using Fast Fourier Transform algorithms [56,57]. The two images are divided into interrogation windows

from which a prediction velocity vector is deduced by using a cross-correlation function [58]. Then, the instantaneous velocity fields of N images obtained from WiDIM are processed to determine the reduced mean velocity components U_{mean}/U_0 and V_{mean}/U_0, the turbulent intensities $(\overline{u'^2})^{1/2}/U_0$ and $(\overline{v'^2})^{1/2}/U_0$, and the reduced Reynolds stresses $\overline{u'v'}/U_0^2$, with

$$U_{mean} = \frac{1}{N}\sum_{i=1}^{N} U_i \quad \text{(and a similar expression for } V_{mean}\text{)}, \tag{9}$$

$$\sqrt{\overline{u'^2}} = \sqrt{\frac{1}{N}\sum\nolimits_{i=1}^{N}(u_i - U_{mean})^2} \quad \text{(and a similar expression for } \sqrt{\overline{v'^2}}\text{)}, \tag{10}$$

$$\overline{u'v'} = \frac{1}{N}\sum_{i=1}^{N}[(u_i - U_{mean})(v_i - V_{mean})]. \tag{11}$$

The number of images N varies from 240 to 384.

The instantaneous velocity vector fields are then used to calculate the instantaneous vorticity and λ maps. Vortices are then detected by applying the wavelet analysis described in Section 2.3. For each vortex identified by the wavelet analysis, the previous treatment provides the center location (x_0, y_0) and the diameter D_v. Cartesian indices (i_v, j_v) of the points belonging to a given vortex are deduced from the condition $r = \sqrt{(x - x_0)^2 + (y - y_0)^2} \leqslant D_v/2$ and the vortex characteristics are then computed:

vorticity peak,

$$\Omega = \max_{i_v, j_v}(\omega); \tag{12}$$

circulation,

$$\Gamma = \oint \boldsymbol{V} \cdot \mathrm{d}\boldsymbol{l} = \int\int \omega \,\mathrm{d}S \quad \rightarrow \sum_{i_v}\sum_{j_v} \omega \Delta x \Delta y; \tag{13}$$

enstrophy,

$$E = \int\int \omega^2 \,\mathrm{d}S \rightarrow \sum_{i_v}\sum_{j_v} \omega^2 \Delta x \Delta y; \tag{14}$$

transport velocity,

$$u_c = u(x_0, y_0) \quad \text{and} \quad v_c = v(x_0, y_0). \tag{15}$$

The integration in expressions (13) and (14) is carried out over the vortex core. A small percentage of vorticity or enstrophy is omitted. This has little influence on the results. On the other hand it is important to deal with compact vortices.

A statistical analysis of these characteristics is developed in Section 4.4.

3.3. Control system

To achieve control, it is first important to select a suitable class of algorithms. The controller structure naturally depends on the instability phenomenon which is considered or on the model used to describe the phenomenon.

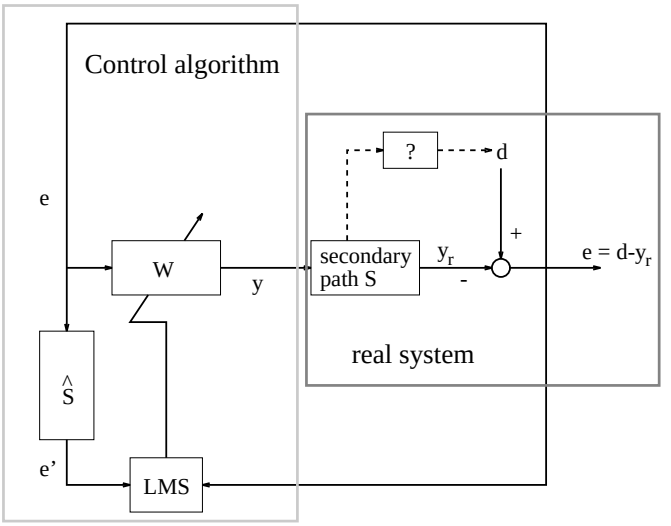

Fig. 6. Noise-source controller with filtered-X LMS update of the coefficients of $\boldsymbol{W}$. The numerical filter $\hat{\boldsymbol{S}}$ is an estimate of the physical system $\boldsymbol{S}$.

Without an a priori knowledge of the system dynamics, one may try to use anti-noise principles. The aim of the control is to counteract the pressure signal in the device (the primary noise). The acoustic signal generated by the controller is superposed to the primary noise and the resulting signal vanishes in the optimal case. Anti-noise algorithms are commonly used in the domain of acoustics and work well in a large variety of applications (see for example the books of Nelson and Elliot [45], and Kuo and Morgan [46]).

If one assumes that the controller action influences the source of perturbation (the organized vortex shedding in the present case), a different type of algorithm may be devised [59]. It is referred to as the Noise Source Control algorithm (NSC) and represented schematically in Fig. 6. While a physical model of this action is not needed for control as indicated in Fig. 6 by a question mark symbol, it is useful to give a qualitative description of how the system works. A possible model for the instability phenomenon and its interaction with the controller is sketched in Fig. 7.

The secondary path $\boldsymbol{S}$, the system "seen by the controller", may be described by a cascade of sub-models: $\boldsymbol{S}1$ represents the path from the controller output to the shear layer origin behind the first baffle, $\boldsymbol{S}2$ is the path connecting the vortex shedding at the baffle to the pressure transducer and $\boldsymbol{S}3$ finally stands for the path relating the transducer to the input of the control algorithm.

Vortex shedding is at the "origin" of the pressure fluctuations but it is also sensitive to the acoustic signal which triggers the periodic shedding. The phenomenon is of the closed-loop type, it is self-sustained and under appropriate conditions its amplitude will grow until non-linear effects bring it to a limit cycle. The acoustic signal d^* acts on the natural uncorrelated vortex shedding (determined by the flow speed U) and produces regular vortex structures and related, nearly periodic, velocity fluctuations u'. Vortex impingement on the downstream obstacle constitutes a

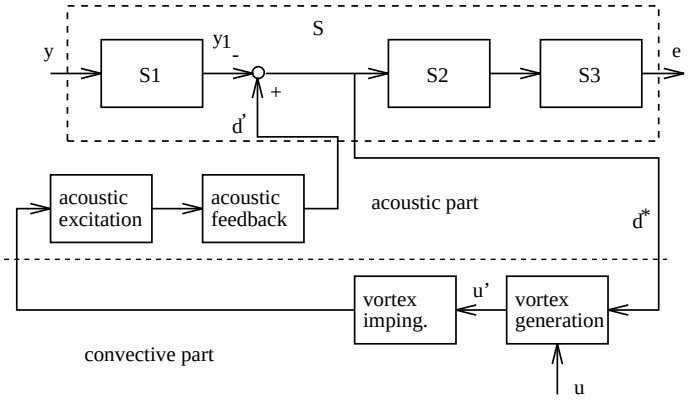

Fig. 7. Detailed secondary path with model of the aeroacoustic phenomenon.

source of acoustic excitation. This source signal feeds energy into one of the system modes. In turn, the velocity fluctuation induced at the baffle produces the signal d' which acts on the shear layer origin and the feedback loop is closed.

This loop involves acoustic and convective motions. The controller signal y_1 injected into the loop at the acoustic level combines with d' to reduce d^* (see Fig. 7). When d^* is effectively reduced, vortex shedding becomes less organized and the self-sustained loop is detuned until d^* is small enough to prevent the periodic shedding of vortices. An essentially broadband acoustic noise prevails in that circumstance. A small controller output will then be sufficient to maintain control, i.e., to keep the acoustic signal below the limit where the self-sustained loop starts operating.

Before developing the control scheme, it is useful to replace the summing point where d' and y_1 superpose with a summing point outside the secondary path $\boldsymbol{S}$. This is valid if one may consider that the cascaded transfer functions $\boldsymbol{S}2$ and $\boldsymbol{S}3$ act linearly. Now, the noise to control (the primary noise) is denoted as d and the signal coming from the controller (having passed the secondary path) is denoted y_r. The advantage of this transformation is obvious. The complete system $\boldsymbol{S}$ now appears separately and the noise to control is superposed "outside" of $\boldsymbol{S}$. One may then obtain the noise source controller as shown in Fig. 6.

The necessary algorithm differs only slightly from a classical anti-sound scheme: here, the error signal e is used directly as input to the filter $\boldsymbol{W}$ (see Fig. 6). This appears appropriate since the microphone signal is assumed to be proportional to the noise source. As may be deduced from Fig. 6, if e is small, a small control signal y_r is sufficient to maintain control. When perfect control is achieved, $e = 0$ and one may write successively:

$$\begin{aligned} e &= d - y_r = d - \boldsymbol{SW}e, \\ (I + \boldsymbol{SW})e &= d, \\ e &= \frac{d}{(I + \boldsymbol{SW})}. \end{aligned} \tag{16}$$

A vanishing error signal is only achieved (with bounded filter coefficients $\boldsymbol{w}$) for $d = 0$. Of course this limit cannot be reached, as for $e = 0$, the primary noise cannot be controlled (the output of $\boldsymbol{W}$ would be zero and with zero control action, the instability cannot be controlled). Nevertheless, the controller will reduce the noise and the noise source until the sensor signal becomes broadband.

For a more detailed analysis of the anti-noise and the noise source control algorithm (NSC), refer to Refs. [26,59], where the two approaches are explained in more detail and experimental data obtained in a simplified set-up illustrates their difference. Only the NSC will be used in what follows because it performs better than the anti-sound algorithm. This indicates, that the model of the phenomenon used to design the NSC is more appropriate than the idea of a simple superposition of two acoustic signals, which forms the basis of the anti-sound algorithm.

The controller used (see Fig. 6) consists of an adaptive FIR (finite impulse response) filter. Its coefficients are updated by using the filtered-X LMS algorithm [60]. The secondary path is compensated by filtering the controller input with an estimate of the secondary path $\hat{\boldsymbol{S}}$ before this signal can be used to update the coefficients of $\boldsymbol{W}$. In fact, the task of the controller is to minimize a cost function $\hat{\xi}_k = e_k^2$, which depends on the controller action and therefore on the coefficients $\boldsymbol{w}$ of the adaptive filter $\boldsymbol{W}$. Hence, the coefficient vector $\boldsymbol{w}$ is updated in order to minimize the cost function. Starting with an arbitrary initial set $\boldsymbol{w}_0$, the filter coefficients change at each iteration in the direction of the gradient of $\hat{\xi}_k$ with respect to $\boldsymbol{w}$. This can be written as

$$\boldsymbol{w}_{k+1} = \boldsymbol{w}_k - \mu' \frac{\partial e_k^2}{\partial \boldsymbol{w}_k}. \tag{17}$$

Now, $\hat{\xi}_k = (d_k - \hat{\boldsymbol{S}}_k \boldsymbol{y}_k)^2$ and $\boldsymbol{y}_k = \boldsymbol{W}_k \boldsymbol{e}_k$. Finally, one obtains

$$\boldsymbol{w}_{k+1} = \boldsymbol{w}_k + \mu e_k \underbrace{\hat{\boldsymbol{S}} \boldsymbol{e}_k}_{\boldsymbol{e}'_k}, \tag{18}$$

with $\boldsymbol{w}_k$ denoting the coefficient vector of $\boldsymbol{W}$ and μ representing the convergence factor replaces $2\mu'$, e_k is the instantaneous error signal measured by the microphone and $\boldsymbol{e}_k$ denotes the vector containing the current and older values of the sensor signal. The index k indicates the kth time step. The secondary path $\boldsymbol{S}$ necessary for writing the gradient correctly is replaced by an estimation $\hat{\boldsymbol{S}}$, obtained during the identification procedure before control (see Section 4.1). As the influence of the controller on d^* cannot be specified explicitly, the final values of $\boldsymbol{W}$ cannot be determined as in the anti-sound case. However, systematic experiments show that $\boldsymbol{W}$ converges towards a band pass filter for the frequency of the instability with a certain phasing.

The idea of using an acoustic signal to act at the source of flow instabilities is explored in earlier studies, for example by Ziada [41]. In contrast to this work, in the present experiments the actuator (loudspeaker) is not located close to the noise source, nor directed towards it (see Fig. 8). Nevertheless, using a feedback controller, it will be shown that the pressure fluctuation level may be reduced significantly by acting on the source of instability.

The algorithm used in practice differs slightly from what was presented up to now in this section. In real-time implementations, finite precision effects lead to unconstrained growth of the filter coefficients. This is due to insufficient spectral excitation of the filter by the input signal. This may be alleviated by including a leakage factor in the updating scheme (see, for example,

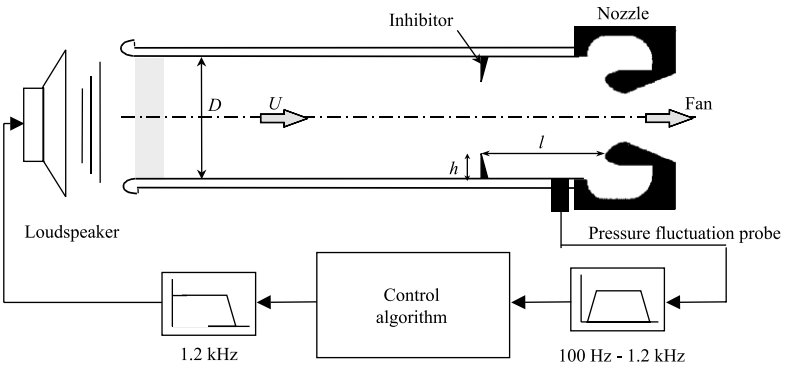

Fig. 8. Sketch of the control system.

Ref. [46]). One may show that this corresponds to adding of low-level white noise to the input signal, which then suffices to obtain the proper spectral excitation of the algorithm. The modified updating algorithm for the controller shown in Fig. 6 is finally given by

$$\boldsymbol{w}_{k+1} = v\boldsymbol{w}_k + \mu \boldsymbol{e}'_k e_k, \tag{19}$$

with $0 < v \leqslant 1$. If the leakage factor $v = 1$, the original updating rule without leak is obtained. More details about the leaky algorithms together with some experimental results for a similar experimental configuration are given in Ref. [26].

4. Experimental results and interpretation

The operating conditions leading to unstable oscillations are discussed in Section 4.1. The identification of the secondary path, which is necessary for successful control is presented in a second step (Section 4.2). Microphone and hot wire signals show the influence of control on the aeroacoustic phenomenon in Section 4.3. A more detailed examination of the effects of control by using particle imaging velocimetry (PIV) is reported in Section 4.4.

4.1. Operating conditions

The instability phenomenon arises from the coupling between acoustics and aerodynamics. The acoustic characteristics of the system determine the frequencies which are prone to be excited by the flow field. The positions of the inhibitor and impingement surface with respect to the eigenmodes further select the frequencies. Finally, the flow speed determines which mode will be excited. Resonant conditions in axial flow configuration are known to appear for small inhibitor–nozzle distances and only for some velocity ranges. In order to get an optimized flow-acoustic coupling, the geometrical parameter l/h (see Fig. 8) is set equal to 8 in the present experiments [61].

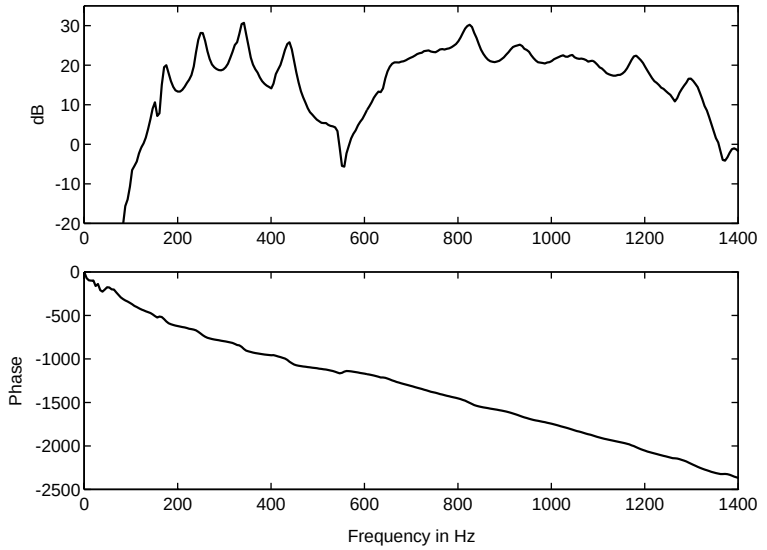

Fig. 9. Identification of acoustic modes. Amplitude (upper plot) and phase (lower plot).

In a first step the acoustic properties, that is the eigenmodes of the device, are determined experimentally. Without flow, the system is excited by a band-limited white noise signal generated by the control algorithm (identification mode). The response of the device is measured by the piezoelectric probe flush mounted on the wall just upstream of the nozzle, considered as an acoustic pressure anti-node thanks to the small section ratio (ratio between the nozzle throat area and the segment cross-section). The complex transfer function between the system response and the white-noise signal is calculated by

$$T_{xy}(f) = \frac{P_{xy}(f)}{P_{xx}(f)}, \tag{20}$$

where P_{xy} is the cross-spectral density from the input of the secondary path to its output and P_{xx} is the power-spectral density of the input signal.

The transfer function amplitude and phase shown in Fig. 9 does not describe the pure acoustic behavior of the system. This transfer function corresponds to the so-called secondary path, that is the "system seen by the control algorithm" (including the filtering, amplification, digital to analog and analog to digital converters,…).

Peaks in the spectrum correspond to higher gain and may be attributed to resonant acoustic modes. This introduces poles in the transfer function and additional phase lag (see the lower plot in Fig. 9). On the other hand, troughs in the amplitude plot correspond to zeros in the transfer function. The phase lead generated in these cases can also be seen in the lower plot in Fig. 9.

Four peaks are identified at 175, 250, 340 and 435 Hz, respectively, in Fig. 9. These correspond to the excitation of the acoustic modes of the test section estimated by

$$f = \frac{(2n-1)c}{4L}, \tag{21}$$

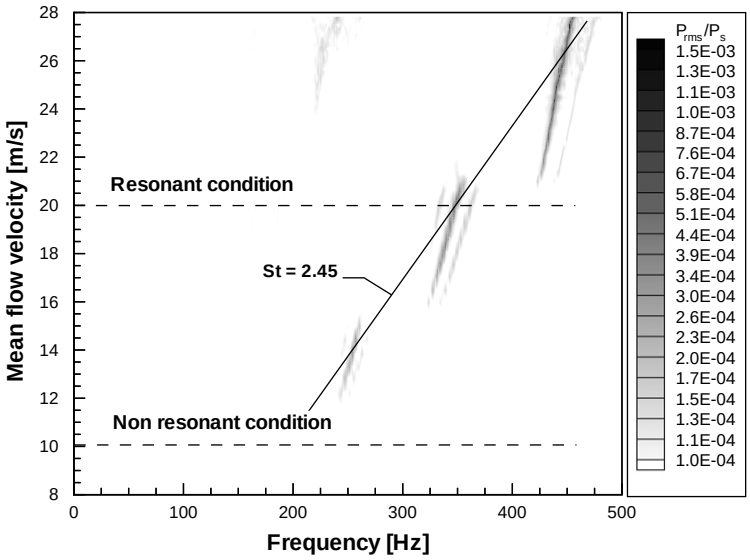

Fig. 10. Contour of pressure fluctuations with respect to the frequency and the mean flow velocity U_0. The pressure fluctuations are normalized by the test section static pressure.

where c is the speed of sound, L is the total length (equal to 1.75 m) and n is the acoustic mode number. This expression is obtained by modelling the test section as an open–closed tube of length L. The acoustic pressure field presents a node at the inlet and an anti-node at the nozzle throat. This structure has been checked by placing eight piezoelectric transducers all along the test section and does not change when the loudspeaker is placed in front of the inlet. Note that expression (21) should depend on the mean flow Mach number ($f = (2n-1)(c/4L)(1-M^2)$) but the velocity U_0 is small compared to the speed of sound and the change in frequency is negligible. Expression (21) predicts theoretical acoustic modes at frequencies of 147, 246, 344 and 442 Hz, respectively, which compare well with experiment.

The aerodynamic response of the system is examined in Fig. 10 by plotting the pressure fluctuation spectrum (normalized by the test section static pressure) with respect to frequency and flow velocity U_0.

In an unconfined configuration, vortex shedding from a bluff obstacle is characterized by a constant hydrodynamic Strouhal number which corresponds to a linear relation between the shedding frequency f and the mean flow velocity U_0:

$$\mathrm{St} = \frac{fl}{U_0} = constant. \tag{22}$$

In confined geometries, as in the present experiments, the acoustic modes of the system influence the vortex shedding. This can be seen in Fig. 10 and also in Fig. 11, which is a simplified 2-D representation of Fig. 10. It contains the previously identified acoustic eigenmodes as horizontal lines and the two most energetic peaks (star and circle symbols) for each velocity U_0 together with their corresponding amplitude. The peaks are normally close to the acoustic

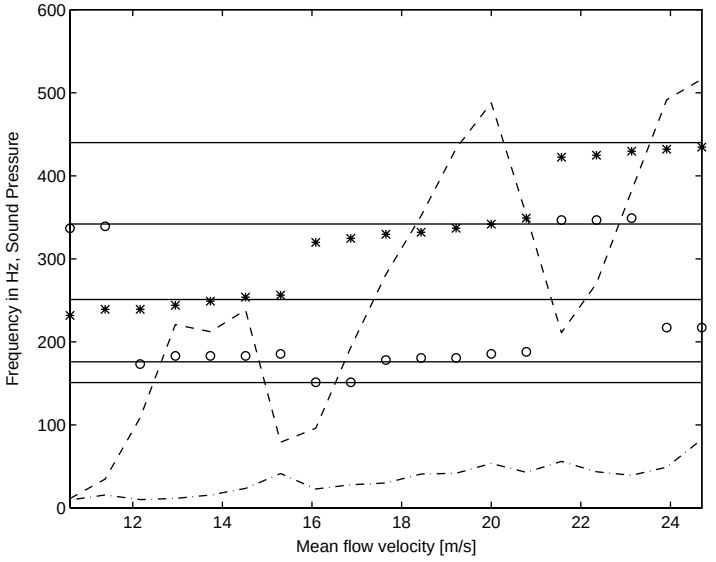

Fig. 11. Coupling of convective modes with acoustics. Horizontal lines: acoustic modes. Frequencies (∗) and corresponding amplitudes (- - - -) of the most energetic modes. Frequencies (◦) and corresponding amplitudes (— · —) for the second-most energetic modes.

eigenmodes. An increase in velocity leads to a slight increase in peak frequency, up to a point, where the excited frequency jumps to another eigenmode. When the shedding frequency is close to one of the acoustic mode frequencies, the amplitude of the pressure fluctuations take large values. The resonance maximum appears when the shedding frequency crosses an acoustic mode frequency. This behavior is typical of coupling between convective and acoustic modes as reported in publications dealing with instabilities in large segmented solid motors [3,14,4]. A more detailed examination of Figs. 10 and 11 shows indeed that the maximum pressure amplitudes for the three different velocity ranges where resonance occurs, correspond to the excitation of three acoustic modes: 251 Hz at $U_0 = 14.4$ m/s, 342 Hz at $U_0 = 20$ m/s, 451 Hz at $U_0 = 26.2$ m/s. These three maxima are located on a line characterized by a constant Strouhal number equal to 2.45 (Fig. 10). This trend is the normal evolution of the Strouhal number as observed in a free hydrodynamic situation, i.e., without influence of acoustics.

These results may be used to define different operating conditions, as indicated in Fig. 10. A non-resonant operation is obtained at a mean flow velocity $U_0 = 10$ m/s, while a resonant response is found for 20 m/s. These two operating conditions cannot be compared directly since the flow and the acoustic conditions change at the same time. To allow a more relevant comparison, the resonance is suppressed by using the active control loop. This defines a third point of operation (same velocity $U_0 = 20$ m/s but without resonance). The efficiency of the adaptive control is clearly identified in Fig. 12. Control reduces the pressure levels whatever the frequency and the velocity. In particular, the peak pressure levels are decreased by 30 dB. The bandwidth of the peaks are also stretched by the control.

Fig. 13 provides the spectrum for the two configurations at 20 m/s. For the resonant response obtained without control, the strong peak in Fig. 13 (solid line) confirms that the vortices are shed

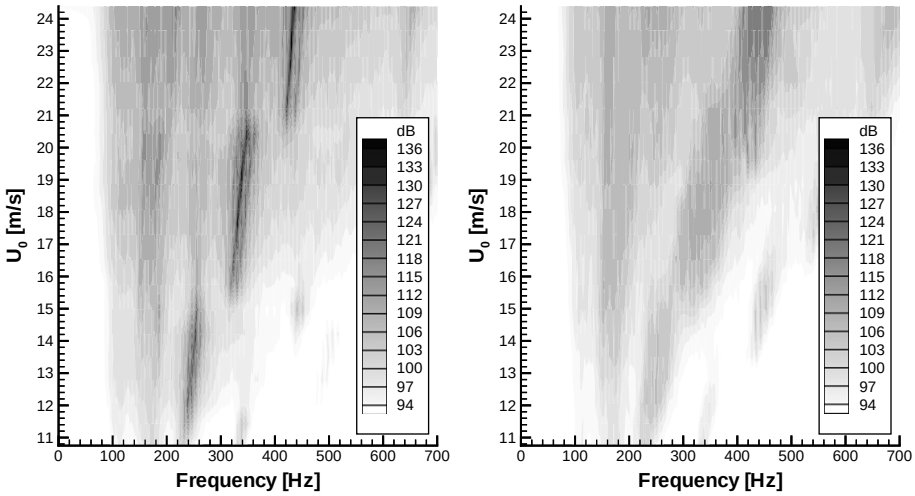

(a) Without adaptive control (b) With adaptive control

Fig. 12. Application of the adaptive control device. Contour of pressure fluctuations with respect to the frequency and the mean flow velocity U_0.

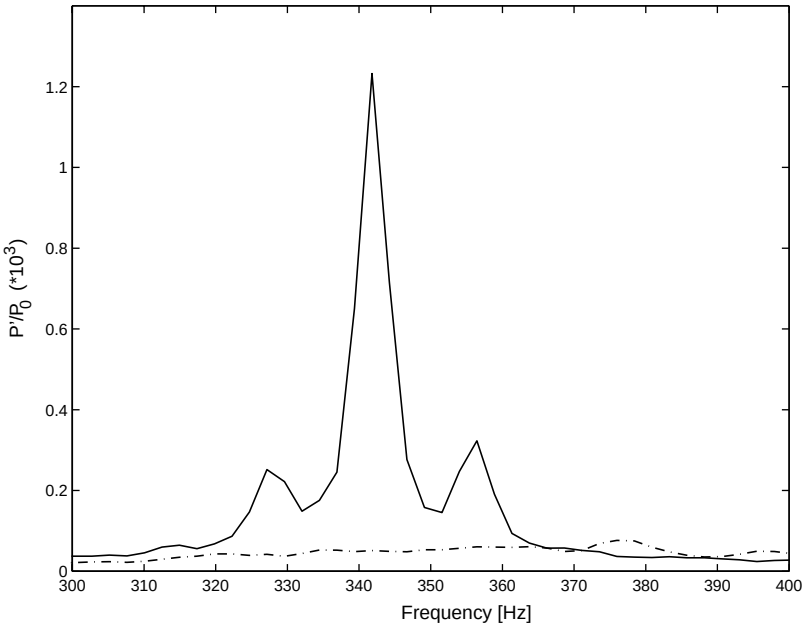

Fig. 13. Spectrum of the pressure fluctuations for $U_0 = 20$ m/s. Resonant case (—, cond. (C)) and with adaptive control (— · —, cond. (B)).

at 342 Hz. The dash-dotted line plot in Fig. 13 shows, that, when using active control, the large pressure fluctuations found under resonance, are strongly damped. The adaptive controller reduces the pressure fluctuations by a factor 20.

Table 1
Parameters of the three PIV configurations

Condition	(A)	(B)	(C)
U_0 (m/s)	10	20	20
Resonance	No	No	Yes
Adaptive control	No	Yes	No
Re_h	12 000	24 000	24 000
f (Hz)	175	342	342
St	2.45	2.45	2.45
p'/p_0 ($\times 10^{-3}$)	0.017	0.06	1.2

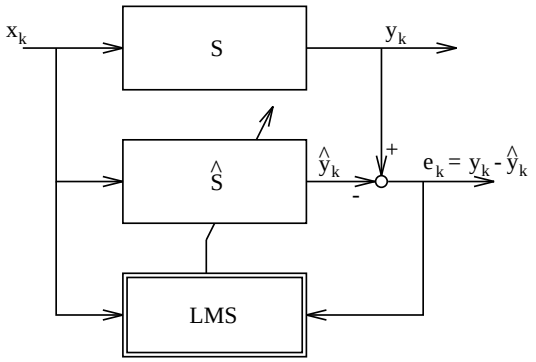

Fig. 14. Adaptive identification of the secondary path $\hat{\boldsymbol{S}}$.

The important parameters of the three different sets of conditions (A), (B) and (C) are summarized in Table 1. The influence of the mean flow velocity will be analyzed by comparing (A) and (B). Comparison of (B) and (C) will allow understanding of the acoustic resonance influence.

4.2. Identification of the secondary path

As shown in Section 3.3, the controller requires some information on the system response. Knowledge of the secondary path $\boldsymbol{S}$ is necessary in order to update the controller coefficients. Identification before control can be used if the secondary path does not change too much during operation; otherwise on-line identification methods might be used to update the estimation of $\boldsymbol{S}$. As the secondary path is mainly acoustic (acoustic actuator, acoustic sensor) in our case, it does not change significantly in the low Mach number range of operation. Identification before control therefore gives a sufficiently accurate estimate of $\boldsymbol{S}$.

In the identification mode, the controller generates a band-limited white noise signal x_k which is delivered to the system and excites the secondary path, as indicated in Fig. 14. The response y_k is measured and compared to the response $\hat{y}_k$ of the adaptive FIR filter $\hat{\boldsymbol{S}}$. The objective during adaptation is to minimize $\hat{\xi}_k = e_k^2$. A sampling frequency of 5 kHz and a FIR filter of 110 elements

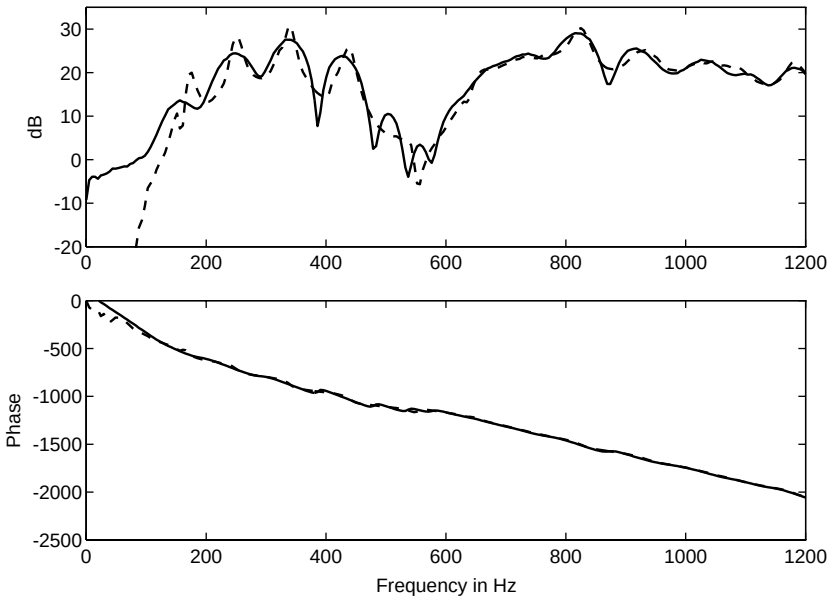

Fig. 15. Adaption of the secondary path, frequency domain. Upper plot: amplitudes. Lower plot: phases. Estimated (—) and real values (- - -).

is used in this example. After adaptation, one compares the behavior of $\hat{\boldsymbol{S}}$ to the real secondary path. In the frequency domain, Fig. 15 shows that the agreement in terms of the amplitude (upper plot) is fair, but the model turns out to be sufficient. The phase introduced by $\hat{\boldsymbol{S}}$ is in fact more important than the amplitude. If the filtering of e by $\hat{\boldsymbol{S}}$ (refer to Fig. 6) leads to a phase error (with respect to the real $\boldsymbol{S}$) of more than $\pm 90^{\circ}$, the adaption of $\boldsymbol{W}$ will fail. Fig. 15 indicates that the phase is well retrieved. The coefficients of $\hat{\boldsymbol{S}}$ are fixed and the loop may be switched to the "controller mode".

4.3. Analysis of pressure and hot wire signals

Before analyzing PIV measurements for the three operating conditions identified in Section 4.1, a broad range of mean flow velocities is examined first by using pressure and hot wire data only.

It will be useful in this study to estimate the acoustic power needed for control. This task would be easier if one were dealing with anti-sound, since the primary noise would stay constant and the controller signal would then give the level of acoustic power injected in the system. In the present situation, the task becomes more complicated as the perturbation level itself changes during control. To get an estimate of the acoustic power injected one may use the controller output as input to the estimated secondary path. Filtering y by $\hat{\boldsymbol{S}}$ provides an estimate of y_r (see Fig. 6). The output signal called *srd* serves as an evaluation of the signal injected into the system. Its spectral density will be plotted together with those of the pressure signals with and without control. In the limit of a precise estimate $\hat{\boldsymbol{S}}$ and if $\hat{\boldsymbol{S}}$ does not change during operation, this estimate suitably

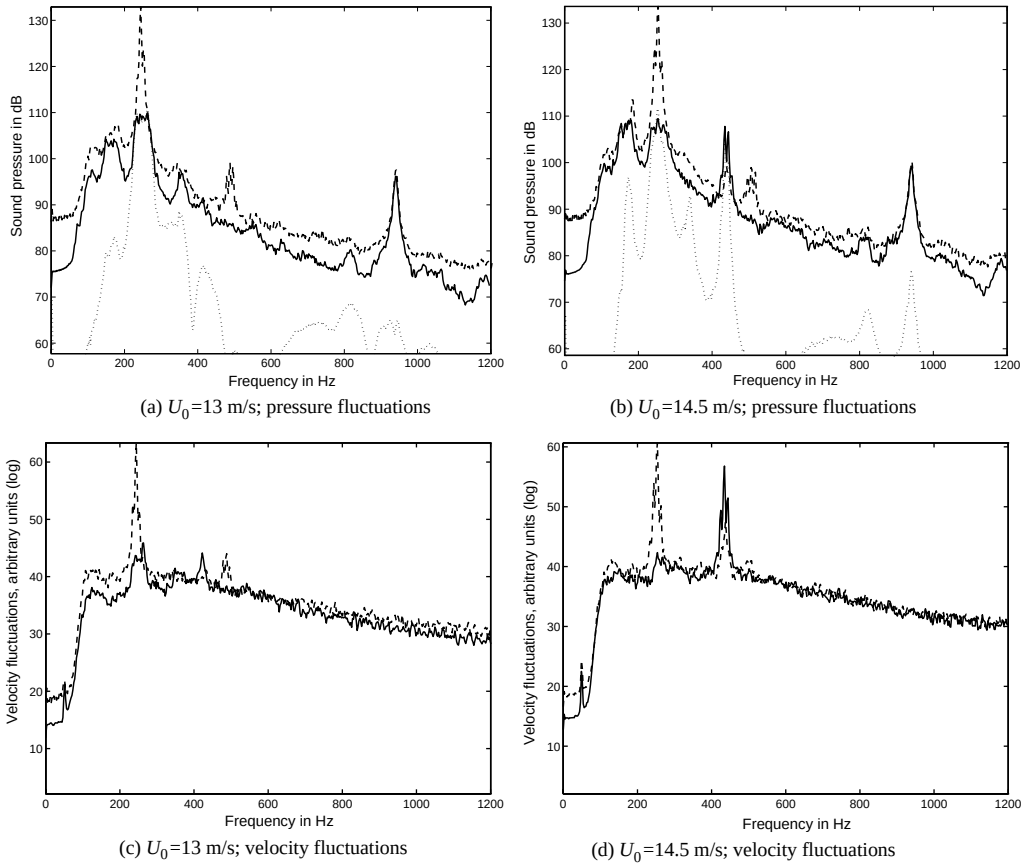

(a) U_0=13 m/s; pressure fluctuations

(b) U_0=14.5 m/s; pressure fluctuations

(c) U_0=13 m/s; velocity fluctuations

(d) U_0=14.5 m/s; velocity fluctuations

Fig. 16. Mean flow velocity = 13 and 14.5 m/s. Spectrum without control (- - - -), with control (—) and *srd*(⋯⋯, only for the pressure).

represents the acoustic signal introduced by the controller and it can be compared to the pressure fluctuations measured by the transducer.

For a mean flow velocity of 13 m/s, power-spectral densities without (dashed line) and with control (solid line) are shown in Fig. 16(a) for the pressure together with the estimated *srd* spectrum (dotted line), and in Fig. 16(c) for the velocity signals. The main peak in the pressure spectrum is reduced by more than 20 dB. The level of *srd* suggests, that the system does not operate in the anti-sound control mode, but that the acoustic signal introduced by the controller is of the order of the remaining noise at the instability frequency. The hot wire signal clearly shows a reduction in the periodic fluctuations of about 15 dB. One may thus conclude that periodic vortex shedding at 240 Hz is strongly reduced. Indeed, velocity fluctuations introduced by an acoustic signal are about an order of magnitude smaller in our case than hydrodynamic velocity fluctuations; hence, the hot wire essentially measures hydrodynamic perturbations.

The pressure spectral density for $U_0 = 14.5$ m/s is shown in Fig. 16(b). Again, by using active control, the pressure signal can be reduced by more than 20 dB. Although a peak appears at 430 Hz under controlled operation, its level remains smaller than the main peak of the controlled

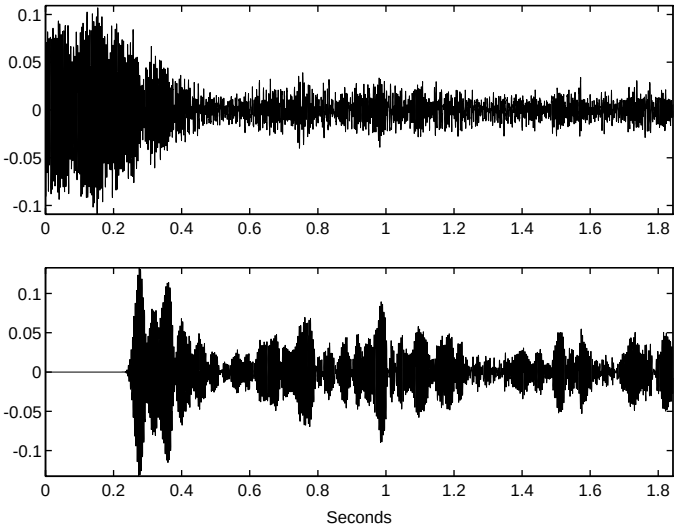

Fig. 17. Time history of the pressure signal, $U_0 = 14.5$ m/s. Vertical line: control switch-on. Upper plot: pressure signal, lower plot: controller output.

spectrum. One may note that this peak also appears in the hot wire spectrum (Fig. 16(d)), where the instability at 240 Hz disappears almost entirely, but the 430 Hz component becomes nearly as important in the controlled spectrum as the initial peak without control. This phenomenon observed in similar situations is attributed to the hydrodynamic response of the flow: in cases where the acoustic feedback is absent, the flow field may still be organized at certain flow speeds and the natural instability of the sheared flow will feature organized structures (this interpretation is supported by numerical simulations carried out in a similar geometry).

Examination of the time history of the pressure signal confirms, that there is a notable reduction in amplitude after the controller switch-on (see Fig. 17, upper plot). The output signal (lower plot in Fig. 17) indicates, that the controller acts at the source of instability. After switch-on, the output increases rapidly above the level which, is, later on, necessary to maintain control. In a pure anti-sound situation where the pressure level stays constant, the controller output would grow up to a constant level which is necessary to generate the anti-sound. In the present situation the large amplitude at the beginning is necessary to break the feedback loop. After that, a relatively small signal is sufficient to prevent the coupling of regular vortices with the system modes.

The acoustic power in the system with and without control may be calculated and compared with the acoustic power needed for achieving control. The power flowing through the duct may be estimated by integrating the acoustic energy flux $\mathscr{F} = p\boldsymbol{v}$ over a cross-section Ξ. One may use for example the duct cross-section containing the pressure transducer. To be precise, one should use the acoustic velocity $\boldsymbol{v}$ to calculate the flux $\mathscr{F}$. This variable is not available and for this reason the approximation $\boldsymbol{v} \approx p/\rho_0 c$ is used. One may then write

$$W_p = \int_{\Xi} \int_0^{f_c/2} \frac{S_{pp}(f)}{\rho_0 c} \, \mathrm{d}A \, \mathrm{d}f. \tag{23}$$

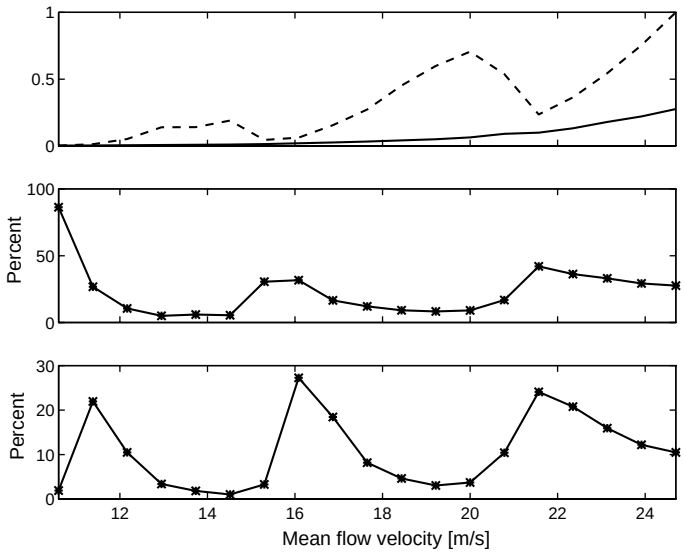

Fig. 18. Comparison of the noise power with (—)/without (- - -) control, normalized values (at the top), remaining power after control with respect to uncontrolled noise in per cent (in the middle) and comparison *srd*/without control, in per cent (at the bottom).

The power appears as an integral over the control surface and a sum over all frequencies of $S_{pp}(f)$, the power-spectrum estimate, expressed in $(\text{Pa})^2/\text{Hz}$. The values of ρ_0 and c are those of air at ambient temperature.

The top graph in Fig. 18 shows the normalized acoustic power without (dashed line) and with control (solid line). The middle graph displays the remaining power after control with respect to uncontrolled noise. Reductions of up to 90% are obtained in certain operating areas. For large flow velocities the actuator is not sufficiently powerful and the reductions are less important than theoretically possible. The acoustic power used during control with respect to the uncontrolled level is shown in the bottom plot of Fig. 18. The effectiveness of control varies, but the remaining power always reaches values below about 5% for conditions, where the peak to broadband ratio in the pressure spectrum is large: the controller works best when the pressure fluctuations are well correlated.

4.4. Analysis of PIV measurements

We now examine the structure of the flow field in the three operating conditions defined in Table 1. Comparison of (A) and (B) serves to isolate the effect of flow velocity. Comparison of (B) and (C) emphasizes the influence of resonance at a given flow velocity.

4.4.1. Mean flow

A set of 240 instantaneous images is processed statistically in order to compute the mean flow field and turbulent intensities (Section 3.2).

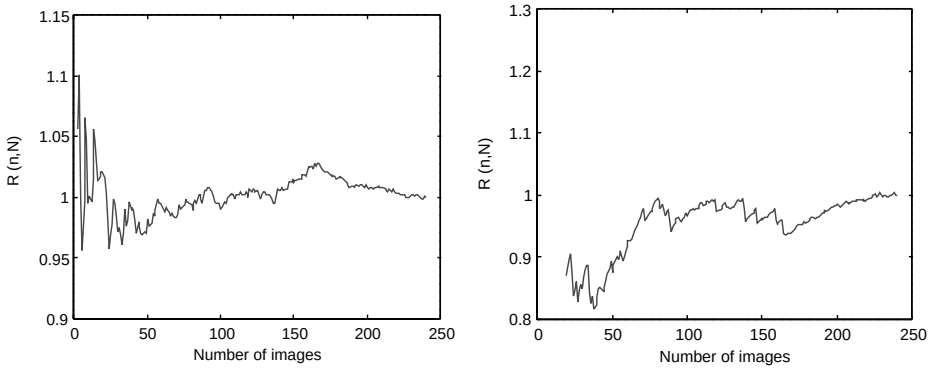

(a) Velocity convergence (b) Turbulent fluctuation convergence

Fig. 19. Statistical convergence of the velocity and turbulent fluctuation for $U_0 = 20$ m/s (without control) and at the point $x/h = 4$ and $y/h = 1.5$.

It is first important to check that the number of images ensures a correct statistical convergence of the averaging process. The average velocity U_{mean} and turbulent fluctuation $(\overline{u'^2})^{1/2}$ are computed at a point located at $x/h = 4$ and $y/h = 1.5$ (in the shear layer). For a number of images n varying from 2 to $N = 240$, one calculates the ratio

$$R(n,N) = \frac{(1/n)\sum_{i=1}^{n} U_i}{(1/N)\sum_{i=1}^{N} U_i} \text{ (and similarly for } \sqrt{\overline{u'^2}}). \tag{24}$$

Fig. 19 indicates that the fluctuation of $R(n,N)$ does not exceed 2% for the velocity, and 5% for the turbulent fluctuation when $n > 150$.

Fig. 20 displays the mean velocity field for the three test cases. The co-ordinates x and y have their origin at the bottom right edge of the inhibitor and h is the inhibitor height. The recirculation bubble generated by the separation of the flow at the top of the inhibitor is revealed by the streamline plot. The influence of the velocity and acoustic conditions on the mean flow may be examined by comparing the positions of the recirculation bubble centers (x_c, y_c). Table 2 lists the results.

Tests carried out with an inhibitor–nozzle distance of 420 mm($l/h = 27$) have shown that the length of the recirculation bubble behind the inhibitor is approximately equal to $12h$ [54]. For the shorter distance used in this experiment ($l/h = 8$), the recirculation bubble cannot extend to $12h$, but is limited to $8h$. For the non-resonant cases (cond. A and B), the recirculation spreads over the region between the inhibitor and the nozzle and the attachment point is probably located on the nozzle head, as sketched in Fig. 21(a). The recirculation length does not depend on the mean flow velocity, as shown in Fig. 20 and Table 2. Under resonant conditions (C), the recirculation bubble center moves upstream. The bubble is more compact than in the non-resonant case and the attachment point is probably not located on the nozzle head (Fig. 21(b)). A possible explanation of the bubble size reduction can be found in the nozzle cavity effect. It is shown in Ref. [28,53] that the nozzle cavity acts as an amplifier of the pressure fluctuations. Without the cavity, the resonance is damped. Indeed, when resonance occurs, the nozzle cavity induces large velocity

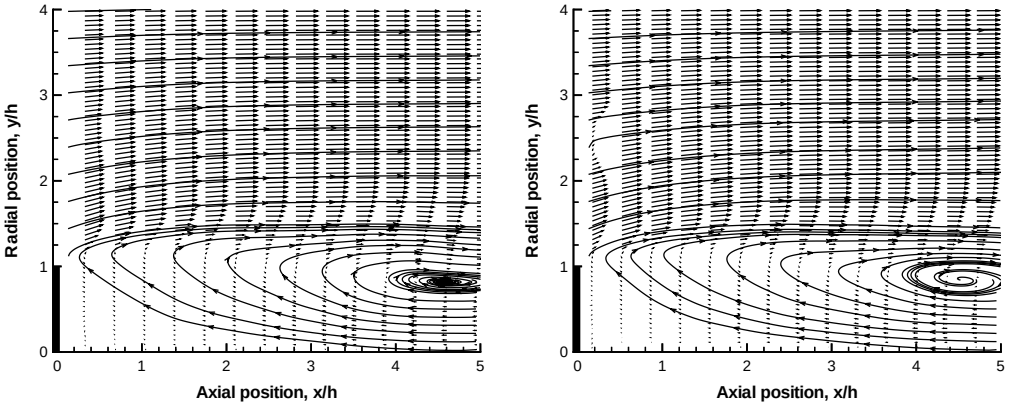

(a) Cond. (A) -non – resonant case (U_0=10 m/s)

(b) Cond. (B) -with adaptive control (U_0=20 m/s)

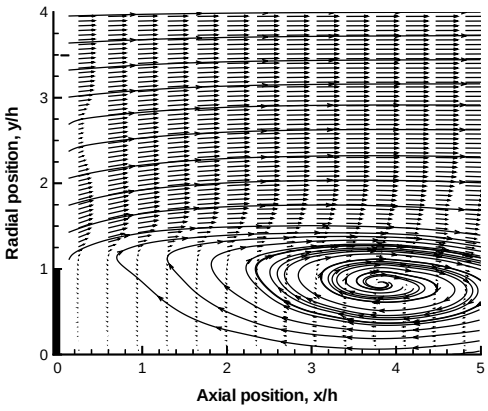

(c) Cond. (C) -resonant case (U_0=20 m/s)

Fig. 20. Mean flow, velocity vectors and streamlines (average on 240 images).

Table 2
Comparison of the position of the recirculation bubble center (x_c, y_c)

Condition	(A)	(B)	(C)
U_0 (m/s)	10	20	20
Resonance	No	No	Yes
Adaptive control	No	Yes	No
x_c/h	4.56	4.53	3.93
y_c/h	0.82	0.85	0.83

fluctuations at the cavity inlet. These fluctuations probably induce oscillations of the recirculation bubble and an upstream shift of its center. The elevation of the bubble center y_c is also influenced to a lesser extent.

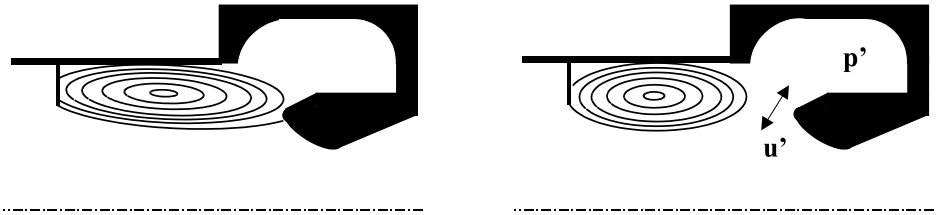

(a) Non−resonant configuration (b) Resonant configuration

Fig. 21. Schematic of the recirculation bubble in the non-resonant and resonant cases at $U_0 = 20$ m/s.

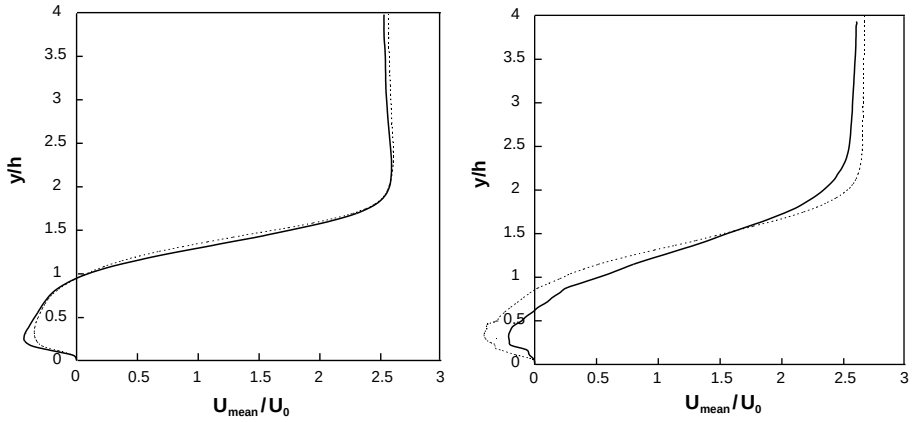

(a) x/h=3 (b) x/h=4.5

Fig. 22. Velocity profiles in the non-resonant (⋯⋯) and resonant (—) cases at $U_0 = 20$ m/s (average on 240 images).

Velocity profiles are plotted in Fig. 22, for two distances from the inhibitor and for non-resonant and resonant cases (B and C). The maximum velocity value denotes the importance of the vena contracta effect. The mean flow behavior is not modified by acoustic resonance for small values of x/h ($x/h<3$). For larger x/h, profiles differ. Resonance reduces the mean velocity gradients in the shear layer. Acoustic oscillations essentially influence the downstream part of the recirculation bubble.

Fig. 23 shows the contours of turbulent fluctuations $(\overline{v'^2})^{1/2}$ of the vertical component of the velocity for the three flow conditions. Averaging is carried out over 240 images and the fluctuation levels divided by the mean flow velocity U_0 are shown for each case in Fig. 23. The maps reveal the wake shear layer geometry. The fluctuations for $U_0 = 10$ and 20 m/s (cond. A and B) are similar in normalized amplitude and distribution. The acoustic resonance increases the level of fluctuation of the flow: the fluctuation of vertical velocity is 30% larger for condition (C). This result was already observed in Section 4.3 where the hot wire spectrum levels with control were less than those obtained without control (Fig. 16). The hot wire signal clearly shows that the periodic vortex shedding at 240 Hz is strongly reduced. This frequency domain information is not

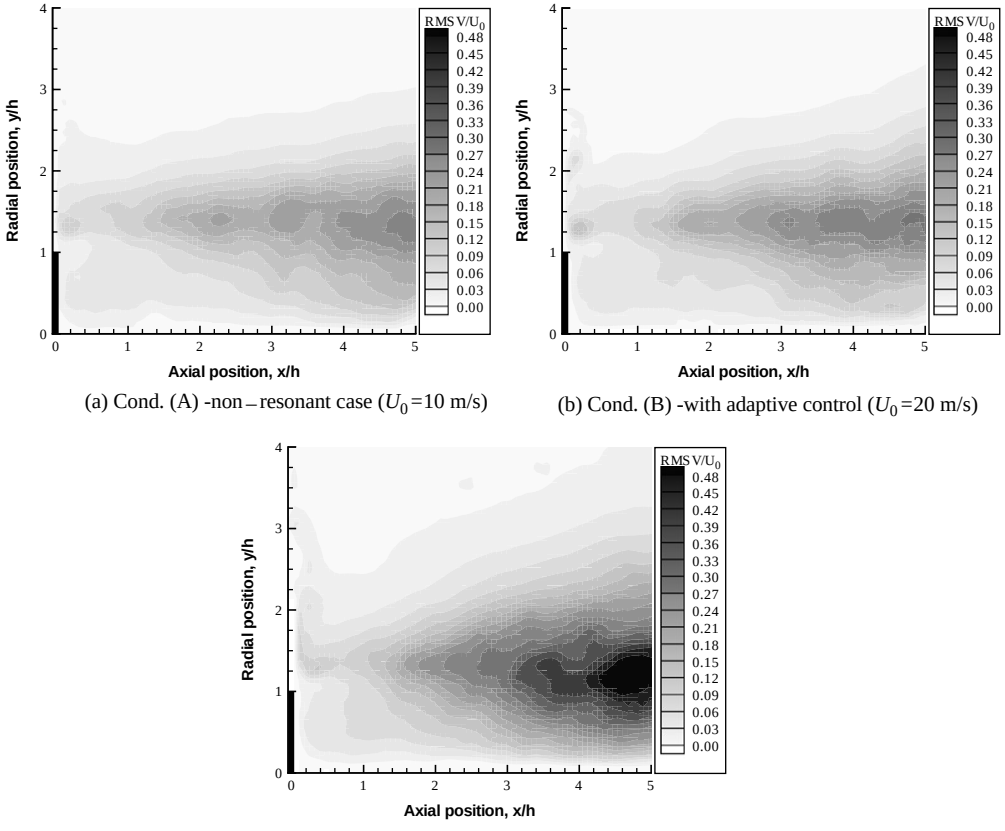

(a) Cond. (A) -non – resonant case (U_0=10 m/s)

(b) Cond. (B) -with adaptive control (U_0=20 m/s)

(c) Cond. (C) -resonant case (U_0=20 m/s)

Fig. 23. Contours of turbulent fluctuations $\sqrt{\overline{v'^2}}$ (average on 240 images).

accessible from the PIV measurements. So, there is still a vortex shedding at a frequency around 240 Hz but its energy has decreased when resonance is eliminated. Intuitively, one may guess that this is due to a change of the coherent structures characteristics. This is where PIV may bring additional information on the full instantaneous flow fields and on the vortex characteristics. The two measurement techniques (hot wire and PIV) are complementary: the hot wire provides the vortex shedding frequency and corresponding spectral amplitude while PIV gives the vortex characteristics as discussed below.

4.4.2. Vortex characteristics

The following analysis relies on the vortex identification method based on a wavelet transformation of the λ field, as explained in Section 2. Processing of an instantaneous PIV image is exemplified in Fig. 24. From the velocity vector field, the vorticity and the λ fields are computed, and then analyzed with the wavelet program. Four vortices are found in the vorticity field. The two structures located near the image border, with center co-ordinates (0.1, 2.1) and (4.6, 1.7), do not correspond to vortices. The first results from vorticity induced by "wrong"

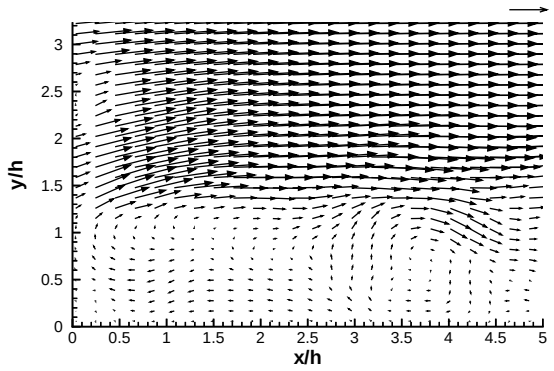

(a) Instantaneous velocity vector field

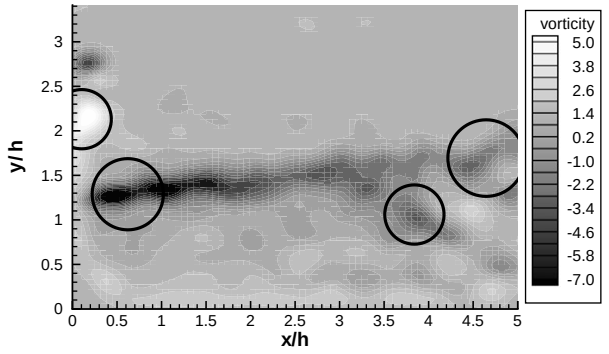

(b) Wavelet analysis applied on vorticity field

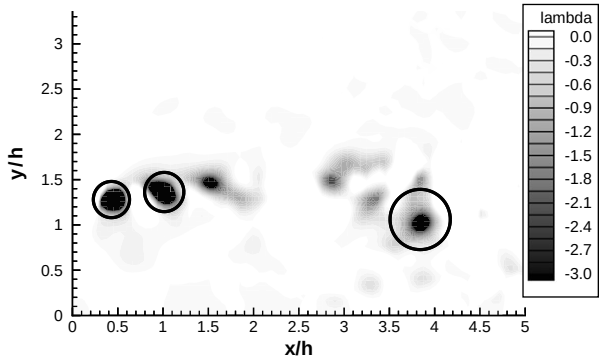

(c) Wavelet analysis applied on λ field

Fig. 24. Example of wavelet analysis on the vorticity and the λ fields. The circles indicate the vortices detected by the analysis.

vectors, due to the local low quality of the PIV image. For the second one, there is a positive gradient $\partial u/\partial y$ larger than $\partial v/\partial x$. This generates a peak of vorticity, and the wavelet responds to this local gradient distribution. Because of the definition of the eigenvalue λ, these two "spurious" vortices are not detected by the second method of analysis. In general, the size of a vortex imbedded in a shear layer is overestimated by the wavelet processing when applied to the vorticity

Table 3
Number of velocity fields recorded, and number of vortices found

Condition	No. of images	Total no. of vortices
(A) $U_0 = 10$ m/s, no resonance	320	1045
(B) $U_0 = 20$ m/s, no resonance	384	1078
(C) $U_0 = 20$ m/s, resonance	368	1128

field. Such a drawback results from the spreading and the additional offset provided by the shear layer itself; this artifact is eliminated by the wavelet-λ scheme.

The wavelet-λ code was automated to allow extensive application to all the images recorded for the three flow conditions. Table 3 gives the number of velocity fields analyzed for each test configuration, and the number of vortices detected.

Analyzing the spatial distribution of the vortices provides a first insight. All the vortices detected by the wavelet-λ scheme are plotted as small circles in Fig. 25. As the downstream distance increases, the vortex positions occupy a broader region, a net result of the nozzle cavity effect which induces vertical velocity fluctuations. As anticipated the scatter in position is enhanced under resonant conditions (C) (Fig. 25(b)).

The data analysis can be pushed further by splitting the domain into sub-regions of length equal to h. Five such areas are selected. They are located at $x/h = 0.5$, 1.5, 2.5, 3.5 and 4.5, respectively. In each sub-region, the vortex characteristics are averaged. Such a procedure has already proved to be an appropriate technique to analyze vortical flow described by PIV data [62,63]. As an example, it is worth pointing out that for each sub-region, the standard deviation of the vortex diameter does not exceed 31% of the average value so that the representative vortex can be regarded as a relevant feature of the flow instability.

The statistical validity of the procedure is assessed by checking the convergence on the basis of a number of images varying from 80 to 368. As an example Fig. 26 shows the evolution of the mean vortex diameter and demonstrates that 240 images are sufficient to achieve good averaging. It is observed that the variation between the average value of vortex properties does not exceed 1% when using 368 images instead of 240.

The axial variation of the vortex properties is outlined in Fig. 27 for the three test conditions (A,B and C). The change in operating conditions induces maximum differences of 15% in the vortex characteristics. In the three cases, the mean vertical vortex position reaches a maximum at $x/h = 2.5$ and then moves towards the wall. The mean trajectory is consistent with the flow pattern shown in Fig. 20, since the vortices follow the streamlines of the mean flow. The vena contracta created by the inhibitor accelerates the flow and curves the streamlines.

Several remarks can be made when following the downstream vortex displacement. The diffusive process reduces the vorticity peak by about 25% and consequently provokes an increase of the vortex size by 20–30%. The circulation first rises and then drops slightly. The 30% decrease of the enstrophy may be explained by the exchange of energy from large to small eddies. The values of the axial transport velocity show that the vortices are slowed down when moving away from the inhibitor. This transport velocity u_v may be related to the local mean velocity U_c determined in the vena contracta at $y/h = 3$ (see Fig. 22). One finds that $u_v \simeq 0.5 \times U_c$. Fig. 28

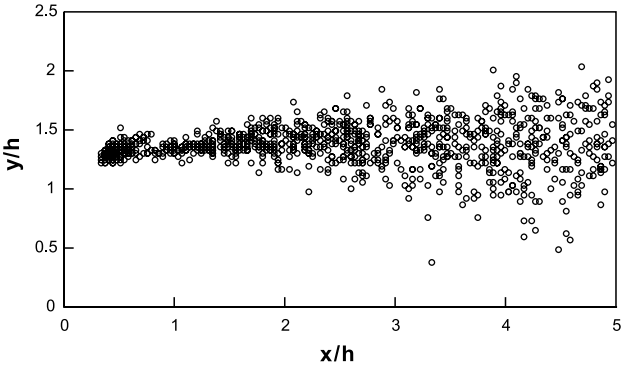

(a) Without resonance (cond. B)

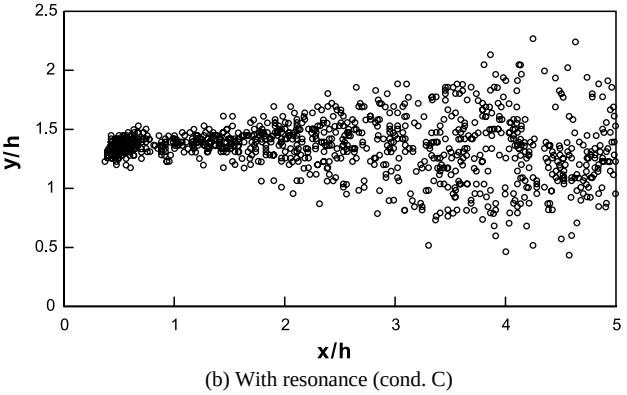

(b) With resonance (cond. C)

Fig. 25. Spatial distribution of the vortices for $U_0 = 20$ m/s.

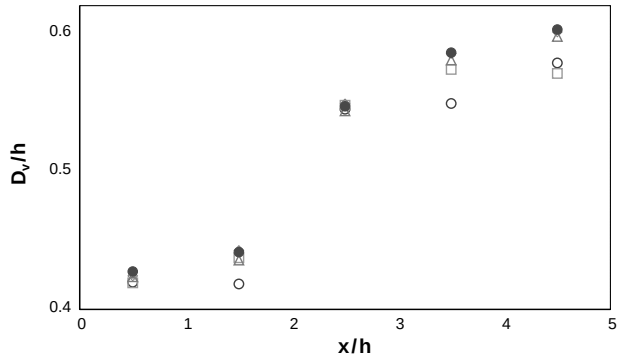

Fig. 26. Convergence for the average diameter for $U_0 = 20$ m/s, resonant. Number of images: 80 (◦), 160 (□), 240 (△), 320 (◇) and 368 (●).

summarizes the previous observations on the basis of the generic Oseen vortex: as the distance from the shedding point increases, the vortices grow in size, lose their energy of rotation, turn at a slower rate and decelerate.

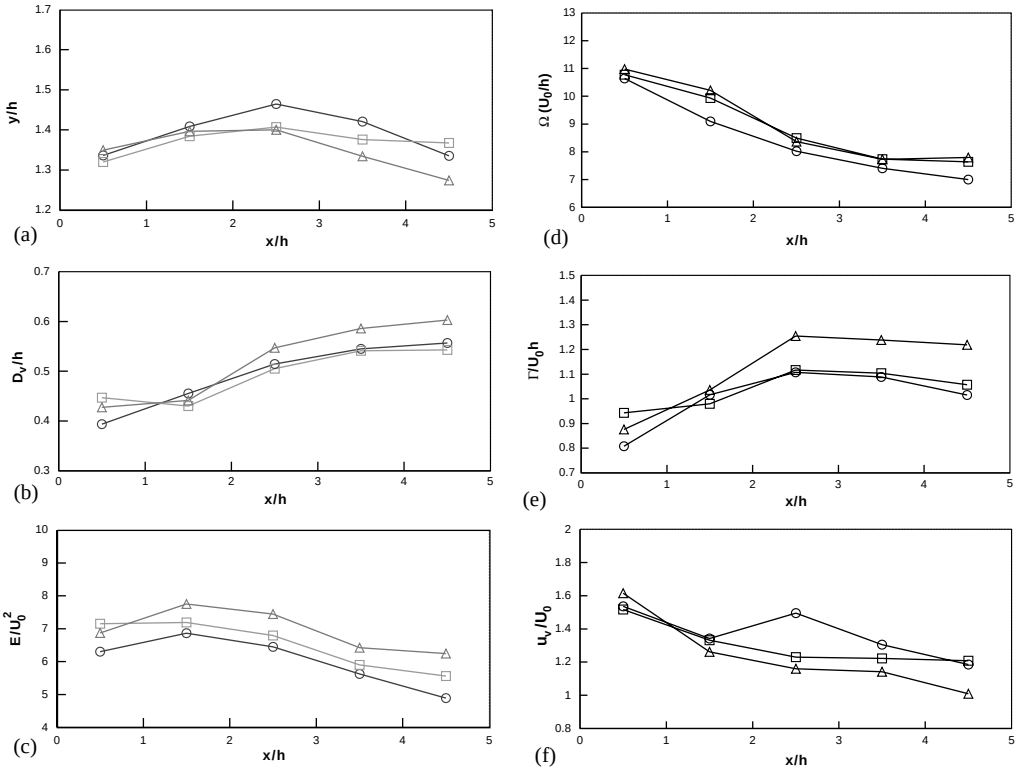

Fig. 27. Group averages of the vortex characteristics in non-dimensional variables for the three configurations. $U_0 =$ 10 m/s without resonance (○), $U_0 = 20$ m/s without resonance (□) and $U_0 = 20$ m/s with resonance (△). (a) average position y/h, (b) average diameter D_v/h, (c) average enstrophy E/U_0^2, (d) average vorticity peak $\Omega/(U_0/h)$, (e) average circulation $\Gamma/(U_0\,h)$, (f) average horizontal component of transport velocity u_v/U_0.

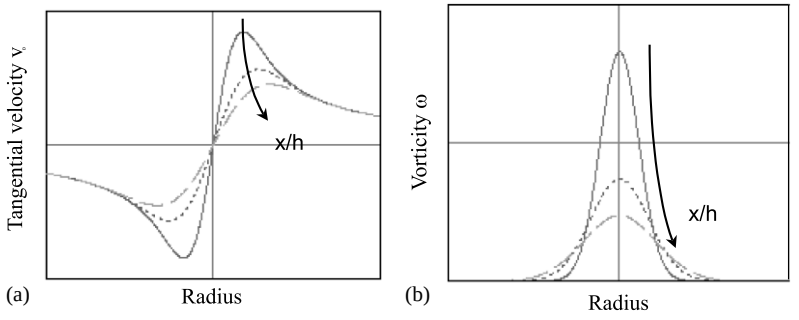

Fig. 28. Evolution of the tangential velocity (a) and vorticity (b) distributions for the generic Oseen vortex as the distance x increases.

As the mean flow velocity increases but under non-resonant conditions, the vorticity peak and the enstrophy rise. The vortex remains of the same size but being slightly more energetic turns faster. In terms of dimensionless quantities, a free-stream velocity variation of 100% leads to a

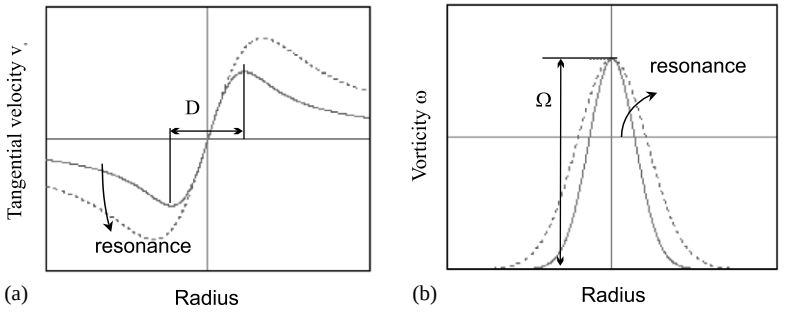

Fig. 29. Evolution of the tangential velocity (a) and vorticity (b) distributions for the generic Oseen vortex under resonant and non-resonant conditions.

change of less than 5% in the vortex characteristics. As shown below, this is definitively smaller than the resonant influence.

The comparison of cases (B) and (C) indicates that resonance causes an augmentation of the diameter, circulation and enstrophy of the vortex by 9%, 12% and 8%, respectively. As indicated in Section 3.2, the circulation and enstrophy are calculated by summing over the vortex cores only. This may have an impact on the absolute values but will not affect the relative changes. The axial transport velocity is reduced by approximately 7% while the vorticity peak is unchanged. Fig. 29 provides a synopsis of the previous observations for the generic Oseen vortex. Under resonant conditions, the vortices grow more rapidly and encompass more energy. They rotate at the same rate but they are advected with a lower velocity.

The circulation is the integral of the tangential velocity v_θ along a contour of the vortex. Using the Oseen vortex model, the tangential velocity is given by $v_\theta = \Gamma/(\pi D_v)$. Under resonant conditions, the tangential velocity which is 5% higher than without resonance, is equal to 13.5 m/s at location $x/h = 3.5$. To see if v_θ is responsible for the vertical turbulent fluctuations observed in Fig. 23, its time average over the vortex shedding period T is evaluated. The procedure consists in postulating that v_θ equals 13.5 m/s during the crossing time t of the vortex: $t = D_v/u_v$, and zero over the remaining time. The time-average tangential velocity is expressed as $v_\theta(t/T) = \Gamma f/(\pi u_v)$ and its value under resonant conditions reaches 2 m/s at location $x/h = 3.5 - y/h = 1.3$. Such a result is consistent with the vertical turbulent fluctuations shown in Fig. 23 which exhibit a peak value of 8 m/s at the same location. Moreover, the standard deviation of the transport velocity is also larger in the resonant case (around 10%). This deviation also contributes to higher $(\overline{v'^2})^{1/2}$-values.

5. Discussion

Interpretation of the data reported in this article may be guided by examining the possible scenarios of resonant flow oscillations (see Fig. 30).

The first scenario emphasizes a direct relationship between the level of pressure fluctuations (acoustic resonance) and the vortex energy content. This is supported by the work

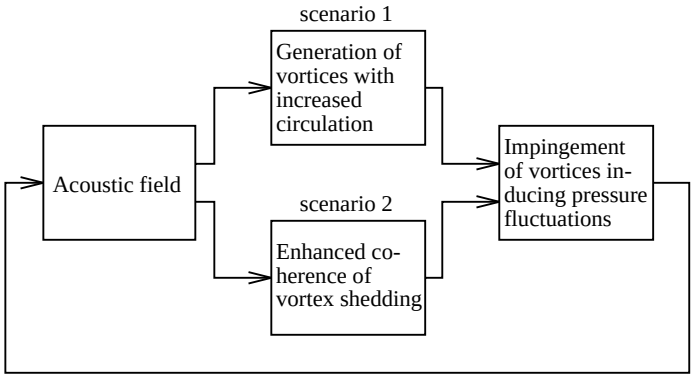

Fig. 30. Two scenarios for aeroacoustic coupling.

of Huang and Weaver [23]. Their flow visualization shows vortices between obstacles in the resonant case, and the absence of structures when active control is applied. In that experiment, active control not only reduces the sound pressure level but also eliminates the vortices in the shear layer. In the first scenario, the acoustic–hydrodynamic coupling induces the coherent vortex generation. The vortex impingement on the downstream obstacle generates the pressure fluctuations.

In the second scenario resonance is obtained when vortex shedding is more coherent. This corresponds to the present experimental observations since vortices are still shed even when acoustic oscillations are essentially cancelled. The vortical structures produce acoustic resonance when the shedding frequency corresponds to an acoustic mode frequency of the system. Then the acoustic–hydrodynamic coupling enhances the correlation of the vortical patterns. However, the small increase in vortex characteristics (energy, circulation) under resonant conditions may not explain the large pressure fluctuations. Therefore, it is conjectured that the pressure fluctuations result from the periodically coherent impingement of the vortices on the nozzle head. In such conditions, the acoustic power is increased (see microphone results, Section 4.3) and influences the vortex shedding by stabilizing its frequency (see hot wire results, Section 4.3). A small amount of this energy is transferred to the vortex explaining why the enstrophy rises only by 10% when resonant conditions are reached. The resonance effect is reinforced by the presence of the cavity in the nozzle. Indeed, Ref. [53] demonstrated a strong effect of the nozzle cavity on the amplification of the pressure fluctuations.

6. Conclusions

The influence of adaptive control on vortex-driven instabilities in a scaled model of solid propellant motors has been investigated using pressure and hot wire signals and PIV measurements. These complementary experimental techniques provide information on the frequency and amplitude of the instability as well as on the properties of the vortical flow.

Three operating conditions are defined to examine the influence of the mean flow velocity and the acoustic resonance on the behavior of the coherent structures. Comparison of two different flow velocities, one naturally non-resonant and one non-resonant under control, emphasizes the influence of the flow speed on the vortex properties. Comparison of a naturally resonant case without and with control singles out the effect of acoustic resonance on the vortex properties.

The experimental data indicate that the pressure level reached under a resonant condition results from a vortex–nozzle interaction. The vortices impinge on the nozzle head more coherently and feed energy into one mode of the system, bringing the fluctuation level to a large value.

The controller scheme and the analysis of the controller signals confirm the action of control at the origin of the noise. The influence of the actuator signal is not limited to its superposition to the resonant acoustic signal. It modifies at the same time the generation of pressure fluctuations.

The resonant condition is characterized by the following: a reduction of the length of the recirculation bubble formed behind the obstacle; an increase of the velocity fluctuations; a decrease of the vertical distance between the vortices and the wall; an increase of the diameter, the enstrophy and the circulation of the vortices but a drop of the vortex transport velocity; no effect on the vorticity peak.

Acknowledgements

This work was supported in part by the European Space Agency (ESA) and by the Centre National d'Etudes Spatiales (CNES). It is a part of a research programme co-ordinated by the CNES and ONERA (Office National d'Etudes et de Recherches Aerospatiales). S. Candel is also professor with Institut Universitaire de France.

References

[1] D.R. Mason, S.L. Folkman, M. Behring, Thrust oscillations of the space shuttle solid rocket booster motor during static tests, American Institute of Aeronautics and Astronautics, Paper 79-1138, 1979.

[2] F.S. Blomshield, Pressure oscillations in post-challenger space shuttle redesigned solid rocket motors, Journal of Propulsion and Power 9 (1993) 217–221.

[3] R.S. Brown, R. Dunlap, S.W. Young, R.C. Waugh, Vortex shedding as a source of acoustic energy in segmented solid rockets, Journal of Spacecraft 18 (1981) 312–319.

[4] K.W. Dotson, S. Koshigoe, K.K. Pace, Vortex shedding in a large solid rocket motor without inhibitors at the segmented interfaces, Journal of Propulsion and Power 13 (1997) 197–206.

[5] F. Vuillot, J.C. Traineau, M. Prevost, N. Lupoglazoff, Experimental validation of stability assessment methods for segmented solid propellant motors, American Institute of Aeronautics and Astronautics, Paper 93-1883, 1993.

[6] M. Prevost, F. Vuillot, J.C. Traineau, Vortex shedding driven oscillations in a subscale motor for the ariane 5 MPS solid rocket motors, American Institute of Aeronautics and Astronautics, Paper 96-3247, 1996.

[7] J.C. Traineau, M. Prevost, F. Vuillot, P. Le Breton, J. Cuny, N. Preioni, R. Bec, A subscale test program to assess the vortex shedding driven instabilities in segmented solid rocket motors, American Institute of Aeronautics and Astronautics, Paper 97-3247, 1997.

[8] G.A. Flandro, H.R. Jacobs, Vortex generated sound in cavities, American Institute of Aeronautics and Astronautics, Paper 73-1014, 1973.
[9] D. Rockwell, E. Naudascher, Review—self-sustaining oscillations of flow past cavities, Journal of Fluids Engineering 100 (1978) 152–165.
[10] D. Rockwell, Oscillations of impinging shear layers, Journal of the American Institute of Aeronautics and Astronautics 21 (1983) 645–664.
[11] J.E. Rossiter, Wind tunnel experiments on the flow over rectangular cavities at subsonic and transonic speeds, Aeronautical Research Council, Ministry of Aviation, Reports and Memoranda 3438, London, 1964.
[12] C.R.W. Tam, P.T.W. Block, On the tones and pressure oscillations induced by flow over rectangular cavities, Journal of Fluid Mechanics 89 (1978) 373–399.
[13] M.S. Howe, Acoustics of Fluid–Structure Interactions, Cambridge University Press, Cambridge, 1998.
[14] R. Dunlap, R.S. Brown, Exploratory experiments on acoustic oscillation driven by periodic vortex shedding, Journal of the American Institute of Aeronautics and Astronautics 19 (1981) 408–409.
[15] F. Vuillot, Votex-shedding phenomena in solid rocket motors, Journal of Propulsion and Power 11 (1995) 626–639.
[16] A. Kourta, Shear layer instability and acoustic interaction in solid propellant rocket motors, International Journal of Numerical Fluid Mechanics 25 (1997) 973–981.
[17] C. Mombelli, A. Guichard, F. Godfroy, J.-F. Guery, Parallel computation of vortex shedding in solid rocket motors, American Institute of Aeronautics and Astronautics, Paper 99-2510, 1999.
[18] J. Anthoine, J.-M. Buchlin, J.-F. Guery, Effect of nozzle cavity on resonance in large SRM: numerical simulation, Journal of Propulsion and Power, submitted.
[19] D. Yildiz, J. Anthoine, J.-M. Buchlin, Influence of radial injected flow on the aeroacoustic coupling in solid propellant boosters, American Institute of Aeronautics and Astronautics, Paper 2001–2101, 2001.
[20] J.-F. Guery, G. Avalon, F. Vuillot, F. Plourde, J. Anthoine, B. Platet, Use of cold flow experiments in the ASSM program: lessons and results, Second European Conference on Launcher Technology, Rome, Italy, November 21–24, 2002.
[21] F.E.C. Culick, K. Magiawala, Excitation of acoustic modes in a chamber by vortex shedding, Journal of Sound and Vibration 64 (1979) 455–457.
[22] K. Hourigan, M.C. Welsh, M.C. Thompson, A.N. Stokes, Aerodynamic sources of acoustic resonance in a duct with baffles, Journal of Fluids and Structures 4 (1990) 345–370.
[23] X.Y. Huang, D.S. Weaver, On the active control of shear layer oscillations across a cavity in the presence of pipeline acoustic resonance, Journal of Fluids and Structures 5 (1991) 207–219.
[24] P. Planquart, B. Alkislar, A. Stubos, C. Benocci, D. Olivari, Cold flow analysis for Ariane 5 P230—experimental investigations, von Karman Institute, Reprint 1995-42, 1995.
[25] J. Anthoine, D. Olivari, Cold flow simulation of vortex induced oscillations in a model of solid propellant boosters, American Institute of Aeronautics and Astronautics, Paper 99-1826, 1999.
[26] M. Mettenleiter, E. Haile, S. Candel, Adaptive control of aeroacoustic instabilities, Journal of Sound and Vibration 230 (2000) 761–789 (doi: 10.1006/jsvi.1999.2659).
[27] A.K. Stubos, C. Benocci, E. Palli, G. K. Stoubos, D. Olivari, Aerodynamically generated acoustic resonance in a pipe with annular flow restrictors, Journal of Fluids and Structures 13 (1999) 755–778 (doi: 10.1006/jfls.1999.0226).
[28] J. Anthoine, J.-M. Buchlin, A. Hirschberg, Effect of nozzle cavity on resonance in large SRM: theoretical modeling, Journal of Propulsion and Power 18 (2002) 304–311.
[29] A. Flatau, W. VanMoorhem, Prediction of vortex shedding responses in segmented solid rocket motors, American Institute of Aeronautics and Astronautics, Paper 90-2073, 1990.
[30] A. Schachenmann, D. Rockwell, Self-sustained oscillations of turbulent pipe flow terminated by an axisymmetric cavity, Journal of Sound and Vibration 73 (1980) 61–72.
[31] D. Couton, F. Plourde, S. Doan, Analysis of energy transfers of a sheared flow generated by wall injection, Experiments in Fluids 26 (1999) 222–232.
[32] H.S. Tsien, Servo-stabilisation of combustion in rocket motors, Journal of American Rocket Society 22 (1952) 256–263.

[33] L. Crocco, S.L. Cheng, Theory of combustion instability in liquid propellant rocket motors, AGARDOGRAPH 8, NATO, Butterworths Science Publication, London, 1956.
[34] F.E. Marble, Servo-stabilization of low-frequency oscillations in liquid propellant rocket motors, Zeitschrift für Angewandte Mathematik und Physik 6 (1953) 1–35.
[35] P. Dines, Active Control of Flame Noise, Ph.D. Thesis, Cambridge University, 1983.
[36] M.A. Heckl, Active control of the noise from a Rijke tube, in: G. Comte-Bellot, J.E. Ffowcs-Williams (Eds.), Aero- and Hydro-acoustics IUTAM, Springer, Berlin, 1985, pp. 211–216.
[37] G.J. Bloxsidge, A.P. Dowling, N. Hooper, P. Langhorne, Active control of an acoustically driven combustion instability, Journal of Theoretical and Applied Mathematics 6 (1987) 161–175.
[38] W. Lang, T. Poinsot, S. Candel, Active control of combustion instability, Combustion Flame 70 (1987) 281–289.
[39] K.R. McManus, T. Poinsot, S. Candel, A review of active control of combustion instabilities, Progress of Energy Combustion Science 19 (1993) 1–29.
[40] K. Roussopoulos, Feedback control of vortex shedding at low Reynolds numbers, Journal of Fluid Mechanics 248 (1993) 267–296.
[41] S. Ziada, Feedback control of globally unstable flows: impinging flows, in: P.W. Bearman (Ed.), Flow-Induced Vibration, A.A. Balkema, Rotterdam, 1995, pp. 579–591.
[42] J.E. Ffowcs Williams, X.Y. Huang, Active stabilisation of compressor surge, Journal of Fluid Mechanics 204 (1989) 245–262.
[43] G. Billoud, M.A. Galland, C.H. Huu, S. Candel, Adaptive active control of combustion instabilities, Combustion Science and Technology 81 (1992) 257–283.
[44] S. Koshigoe, T. Komatsuzaki, V. Yang, Active control of combustion instabilities with on-line system identification, American Institute of Aeronautics and Astronautics, Paper 96-0759, 1996.
[45] P.A. Nelson, S.J. Elliot, Active Control of Sound, Academic Press, New York, 1992.
[46] S.M. Kuo, D.R. Morgan, Active Noise Control Systems, Wiley, New York, 1996.
[47] S.K. Robinson, A review of vortex structures and associated coherent motions in turbulent boundary layers, Proceedings of the Second IUTAM Symposium on Structural Turbulence and Drag Reduction, Zurich, 1989.
[48] F.A.K.M. Hussain, Coherent structures and turbulence, Journal of Fluid Mechanics 173 (1997) 303–356.
[49] J. Jeong, F.A.K.M. Hussain, On the identification of a vortex, Journal of Fluid Mechanics 285 (1995) 69–94.
[50] C. Schram, P. Rambaud, M.L. Riethmuller, Coherent structures eduction downstream of a backward facing step using Particle Image Velocimetry and wavelet analysis, Experiments in Fluids, in press.
[51] M. Farge, Wavelet transforms and their applications to turbulence, Annual Review of Fluid Mechanics 24 (1992) 395–457.
[52] C. Schram, M.L. Riethmuller, Vortex ring evolution in an impulsively started jet using digital particle image velocimetry and continuous wavelet analysis, Measurement Science and Technology 12 (2001) 1413–1421.
[53] J. Anthoine, Experimental and Numerical Study of Aeroacoustic Phenomena in Large Solid Propellant Boosters, Ph.D. Thesis, Université Libre de Bruxelles–von Karman Institute, 2000.
[54] J. Anthoine, D. Olivari, Investigation of flow acoustic coupling in a model of solid propellant boosters, ESA SP 426, 1998, pp. 583–590.
[55] O. Repellin, Etude expérimentale de la propagation de tourbillons, von Karman Institute, Stagiaire Report SR 1998-15, 1998.
[56] F. Scarano, M.L. Riethmuller, Iterative multigrid approach in PIV image processing with discrete window offset, Experiments in Fluids 26 (1999) 513–523.
[57] F. Scarano, Particle Image Velocimetry Development and Application—Investigation of Coherent Structures in Turbulent Shear Flows, Ph.D. Thesis, Universit degli Studi di Napoli "FEDERICO II"–von Karman Institute, 2000.
[58] L.M. Lourenco, Particle image velocimetry, von Karman Institute, Lecture Series "Particle Image Velocimetry", LS 1996-03, 1996, pp. 1–110.
[59] M. Mettenleiter, Contrôle Adaptatif des Propulseurs Segmentés, Ph.D. Thesis, Ecole Centrale Paris, 2000.
[60] B. Widrow, S.D. Stearns, Adaptive Signal Processing, Prentice-Hall, Englwood Cliffs, NJ, 1985.

[61] J. Anthoine, P. Planquart, D. Olivari, Cold flow investigation of the flow acoustic coupling in solid propellant boosters, American Institute of Aeronautics and Astronautics, Paper 98-0475, 1998.
[62] F. Scarano, C. Benocci, M.L. Riethmuller, Pattern recognition analysis of the turbulent flow past a backward facing step, Physics of Fluids 11 (1999) 3808–3818.
[63] O. Repellin, Experimental characterization of vortical structures with aeroacoustic effects, von Karman Institute, Project Report PR 1998-28, 1999.